INTERNATIONAL JOURNAL FOR NUMERICAL METHODS IN FLUIDS
Int. J. Numer. Meth. Fluids 2009; **61**:23–56
Published online 8 December 2008 in Wiley InterScience (www.interscience.wiley.com). DOI: 10.1002/fld.1935

Strategy for spatial simulation of co-rotating vortices

H. Deniau*,† and L. Nybelen

Centre Européen de Recherche et de Formation Avancée en Calcul Scientifique, 42, Avenue Gaspard Coriolis, 31 057 Toulouse Cedex 1, France

SUMMARY

The present numerical study is motivated by the challenge to simulate the three-dimensional spatial dynamics of a co-rotating vortex system, through the development of an elliptic instability (*C. R. Phys.* 2005; **6**(4–5):431–450) using a high-order solver of the compressible Navier–Stokes equations. This phenomenon was studied previously only by temporal simulations. The interest of spatial simulation is first to analyse the effect of the axial velocity on the merging process, which are neglected with the temporal approach, and to study interaction with jet flows. The numerical problem is the choice of boundary conditions (BCs): for the inflow and outflow conditions as well as for the lateral BCs to represent a fluid at rest. Special attention will be paid to the latter because the difficulties come from the non-zero circulation of the vortex system considered. The classic BCs of Poinsot and Lele (*J. Comput. Phys.* 1992; **101**: 104–129) based on the characteristics wave approach have been modified to be more adapted to the physics considered here. This new BC is based on the assumption of an irrotational flow close to the borders (in order to determine the magnitude of the waves), as the vorticity field is concentrated on the computational domain centre where the vortex system is initially placed. After a validation of these improved BCs and of all numerical tools used such as selective artificial dissipation, two spatial simulations of the vortex breakdown phenomenon have allowed validating our solver for a three-dimensional case by comparison with the results of Ruith *et al.* (*J. Fluid Mech.* 2003; **486**:331–378). Thus, the merging process of equal co-rotating vortices through the development of elliptic instability with axial velocity were simulated. Three vortex flow configurations were considered with different vortex systems and velocity peaks ratio (azimuthal and axial velocities).

A numerical tool has been elaborated and validated for the simulation of spatial instability development in vortex flows. The first results show this ability, and the influence of the axial velocity on the dynamics of the instabilities. However, spatial simulations are limited by the computational resources (linked to the resolution and axial domain length to capture the merging process) and restricted to academic vortex flow configuration. Copyright © 2008 John Wiley & Sons, Ltd.

Received 14 March 2008; Revised 13 August 2008; Accepted 21 August 2008

KEY WORDS: boundary conditions; DNS; co-rotating vortices; unsteady flows; spatial simulation; numerical scheme

*Correspondence to: H. Deniau, CERFACS, 42, Avenue Gaspard Coriolis, 31 057 Toulouse Cedex 1, France.
†E-mail: deniau@cerfacs.fr

Contract/grant sponsor: Fundamental Research on Aircraft Wake Phenomena; contract/grant number: AST-CT-2005-012238
Contract/grant sponsor: European Union

1. INTRODUCTION

The wake of an aircraft is composed of several intense vortices, which can persist for a few minutes in the atmosphere. They may be hazardous for following aircrafts encountering the wake, in particular during take-off and landing phases. One needs to characterize the structure of these trailing vortices to develop new concepts to accelerate their decay and reduce the latency time between the landing or take-off of two aircrafts. To that end, the mechanism of this vortex sheet generation between the trailing wake just downstream of the aircraft wing and the vortex system in the far-field (generally composed by a counter-rotating pair) must be studied in detail. The main physical phenomenon occurring in the extended near-field (a few wingspans behind the aircraft) is the merging of the co-rotating vortices generated at flap and wing tip.

This phenomenon has received much attention over the last years by experimental, theoretical and numerical studies. Cerretelli and Williamson [1] have shown in their experiments that this merging process can be decomposed into four stages at low Reynolds numbers. They found that the merging can be explained by the generation of an antisymmetric vorticity field during the process, inducing a velocity pushing one vortex toward the other. Moreover, they showed that the merging time is a function of both the Reynolds number and the initial characteristic ratio a/b, where a is the vortex core size and b the separation distance between the two vortices. Ferreira de Sousa and Pereira [2] confirmed the previous mechanism by using temporal two-dimensional direct numerical simulations. Orlandi [3] investigated the dependence of the merging with Reynolds number and the ratio a/b by spatial three-dimensional DNS. He demonstrated that the merging could be detected by a large increase of pressure extrema and that this three-dimensional merging can be more complex than the one obtained by two-dimensional simulations, the complexity depending largely on the axial disturbances initially imposed on the two vortices. The weak point of the previous simulations is the use of periodic or symmetry boundary conditions (BCs) for the domain faces, which are parallel to the vortex axis. Theoretically, when studying two co-rotating vortices, the total circulation is not equal to zero and imposing periodic or symmetry conditions generates strains on the vortices. To minimize the impact of these boundary effects, large computational domains are employed, which can be out of cost for a three-dimensional DNS [3]. Further, these conditions produce a confinement effect: perturbations injected at the inflow could reflect on these lateral boundaries and impact the vortices, perturbing the simulation of two vortices evolving in a free atmosphere.

The spatial simulation is expected to take into account the curvature of the vortex, which is absent with the temporal one. Indeed, the temporal approach is based on the assumption that the axial gradients are neglected compared to the transverse ones, thus the vortex axis remaining in a plane. The present study aims at bringing all numerical treatments together to perform a space evolving simulation of two co-rotating vortices. In particular, the lateral BCs that are suitable for flows with a non-zero total circulation are investigated.

To define artificial BCs, the concept of non-reflecting BC can be used. Their underlying principle is to cancel the wave entering in the computational domain as proposed by Thompson [4]. Other methods exist to specify a non-reflective BC as proposed by Giles [5] who uses a Fourier decomposition of characteristic waves or by Tam and Dong [6] or Bayliss and Turkel [7] who define radiative BCs for computational aero-acoustics. The main deficiency of these BCs lies in their impossibility to determine incoming waves, which bring physical information into the computational domain. Rudy and Strikwerda [8] propose a partially non-reflecting BC, specifying a static pressure through a subsonic outflow, which is determined by the outside of the computational

DOI: 10.1002/fld

domain. All these approaches are unified by Poinsot and Lele [9], who propose a methodology to take into account physical properties to obtain numerical BCs. Today, there are no artificial BCs available and suitable for all flows, which are at the same time non-reflective and capable to determine physical incoming waves. This deficiency leads to the use of non-perfect BCs, which produce unphysical waves and possibly non-physical solutions [10] in the worst case. To avoid such phenomenon, a classical way is to use a buffer zone or sponge layer, adjacent to the physical domain of interest, where either the equations are gradually modified or the solution is filtered in order to reduce disturbances at the outflow boundary. Colonius [11] proposed an extended review of these techniques that include filtering, relaxation towards a known solution and mesh stretching to render the perturbations decreasingly resolved, hoping that they will be nearly cancelled before reaching the boundary.

This paper is organized as follows: the first two parts describe the compressible Navier–Stokes (NS) equations and the characteristic wave decomposition on which our new boundary treatment is based. All BCs used for the present study are exposed and discussed. After a brief review of other necessary numerical tools such as artificial dissipation or sponge layer, the influence of all the numerical ingredients is presented using simple validation test cases. In particular, the improvement of the lateral and inflow BCs is discussed, as they represent the main difficulty to simulate a vortex dynamics. These conditions constitute a typical feature of a space evolution simulation. Section 6 is devoted to spatial simulations of vortex breakdown phenomenon. In the last section, a first analysis of space evolving simulations is presented and discussed. Three cases are studied with different axial velocities. Until now, to our knowledge except the approach proposed by Orlandi [3] for incompressible flow, all simulations of vortex dynamics (such as the merging process) are based on a temporal approach. For these kind of simulations, the axial velocity is not taken into account, which greatly simplifies the simulation.

2. GOVERNING EQUATIONS

The governing equations are the three-dimensional compressible NS equations, given in their non-dimensionalized formulation, in an orthonormal system and in a skew-symmetric form

$$\frac{\partial U}{\partial t}+\frac{1}{2}\left[\frac{\partial F_x}{\partial x}+\frac{\partial F_y}{\partial y}+\frac{\partial F_z}{\partial z}\right]+\frac{1}{2}\left[u\frac{\partial U}{\partial x}+v\frac{\partial U}{\partial y}+w\frac{\partial U}{\partial z}+\left(\frac{\partial u}{\partial x}+\frac{\partial v}{\partial y}+\frac{\partial w}{\partial z}\right)U\right]$$
$$=\frac{1}{Re}\left(\frac{\partial G_x(U,\nabla U)}{\partial x}+\frac{\partial G_y(U,\nabla U)}{\partial y}+\frac{\partial G_z(U,\nabla U)}{\partial z}\right) \tag{1}$$

with

$$U=\begin{bmatrix}\rho\\ \rho u\\ \rho v\\ \rho w\\ \rho E\end{bmatrix},\quad F_x=\begin{bmatrix}\rho u\\ \rho u^2+p\\ \rho uv\\ \rho uw\\ u(\rho E+p)\end{bmatrix},\quad F_y=\begin{bmatrix}\rho v\\ \rho uv\\ \rho v^2+p\\ \rho vw\\ v(\rho E+p)\end{bmatrix},\quad F_z=\begin{bmatrix}\rho w\\ \rho uw\\ \rho vw\\ \rho w^2+p\\ w(\rho E+p)\end{bmatrix} \tag{2}$$

DOI: 10.1002/fld

$$G_x=\begin{bmatrix}0\\ \tau_{xx}\\ \tau_{xy}\\ \tau_{xz}\\ \beta_x\end{bmatrix},\quad G_y=\begin{bmatrix}0\\ \tau_{xy}\\ \tau_{yy}\\ \tau_{yz}\\ \beta_y\end{bmatrix},\quad G_z=\begin{bmatrix}0\\ \tau_{xz}\\ \tau_{yz}\\ \tau_{zz}\\ \beta_z\end{bmatrix} \tag{3}$$

where

$$\begin{aligned}\beta_x&=u\tau_{xx}+v\tau_{xy}+w\tau_{xz}+\lambda\frac{\partial T}{\partial x}\\ \beta_y&=u\tau_{xy}+v\tau_{yy}+w\tau_{yz}+\lambda\frac{\partial T}{\partial y}\\ \beta_z&=u\tau_{xz}+v\tau_{yz}+w\tau_{zz}+\lambda\frac{\partial T}{\partial z}\end{aligned} \tag{4}$$

and $\tau_{ij}=\mu(\partial u_i/\partial x_j+\partial u_j/\partial x_i-\frac{2}{3}\delta_{ij}\partial u_k/\partial x_k)$ (with summation convention).

The dynamic viscosity μ is given by Sutherland's law. With a constant Prandtl number Pr, the thermal conductivity coefficient can be written as $\lambda=\mu c_p/Pr$ with $c_p=\gamma R/(\gamma-1)$ (perfect gas $R=287\,\mathrm{J/kg\,K}$) the specific heat capacity at constant pressure and for air $Pr=0.72$ and $\gamma=1.4$. All simulations were performed with a Reynolds number Re based on the vortex circulation Γ (except for the simulations presented in the Section 6) and air viscosity v:

$$Re=Re_\Gamma=\frac{\Gamma}{v} \tag{5}$$

In order to close the system, the following two relations must be considered:

$$\begin{aligned}p&=\rho RT\\ \rho E&=\frac{1}{2}\rho(u^2+v^2+w^2)+\frac{p}{\gamma-1}\end{aligned} \tag{6}$$

The use of a skew-symmetric form is motivated by the conservation of the kinetic energy, which preserves from aliasing phenomenon [12].

The NS equations are discretized using the finite difference method, with a sixth-order compact scheme for the convective and diffusive terms. Time integration is performed by a third-order Runge–Kutta method. The computational domain is discretized by a stretched Cartesian mesh. For the computation of the spatial derivatives on this mesh, an extension of the Lele compact scheme [13] is used. The reader is invited to refer to the work by Gamet *et al.* [14] for the formulae. Figure 1 represents the computational domain and its different faces where the BC are applied. At the bottom face a pair of co-rotating vortices is imposed, knowing their properties (circulation and size). For the lateral faces, an original BC generating low perturbations and allowing incoming flow is used. This is motivated by the aim to represent real ambient flow conditions at rest. At the top face, a semi-non-reflecting BC is prescribed, which is based on the Giles theory [5]. All these conditions are based on a characteristic analysis, which is detailed in the next section.

DOI: 10.1002/fld

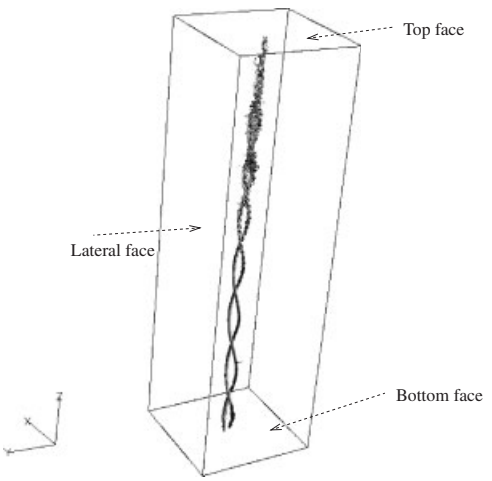

Figure 1. Computational domain for the spatial simulation of a two co-rotating vortex system, governed by the merging process leading to a single vortex.

3. NS-CHARACTERISTIC BCs

3.1. Basic formulation

In order to simplify the expressions, only the boundary at the face $x = x_{\max}$ is considered. The NS equations are reformulated at this face to derive the amplitude of the characteristic waves normal to the boundary. Primitive variables are introduced such as $V = [\rho, u, v, w, p]^{\mathrm{T}}$, and P the matrix $\partial U / \partial V$. The following form of the NS equations is obtained by:

$$\frac{\partial V}{\partial t} + P^{-1} A_x P \frac{\partial V}{\partial x} = P^{-1} S \tag{7}$$

where

$$S = -\frac{1}{2}\left[\frac{\partial F_y}{\partial y} + \frac{\partial F_z}{\partial z}\right] - \frac{1}{2}\left[v\frac{\partial U}{\partial y} + w\frac{\partial U}{\partial z} + \left(\frac{\partial v}{\partial y} + \frac{\partial w}{\partial z}\right)U\right] + \frac{1}{Re}\left(\frac{\partial G_x(U, \nabla U)}{\partial x} + \frac{\partial G_y(U, \nabla U)}{\partial y} + \frac{\partial G_z(U, \nabla U)}{\partial z}\right) \tag{8}$$

and the Jacobian matrix A_x is defined by

$$A_x = \frac{\partial F_x}{\partial U} \tag{9}$$

The matrix $P^{-1} A_x P$ is diagonalizable. Denoting Λ as the diagonal matrix and R as the right eigenvector matrix, Equation (7) becomes

$$R^{-1}\frac{\partial V}{\partial t} + \Lambda R^{-1}\frac{\partial V}{\partial x} = R^{-1} P^{-1} S \tag{10}$$

where $\Lambda = \mathrm{Diag}(u - c, u, u, u, u + c) = \mathrm{Diag}(\lambda_1, \lambda_2, \lambda_3, \lambda_4, \lambda_5)$ and $c = \sqrt{\gamma P / \rho}$ the sound speed.

DOI: 10.1002/fld

The vector defined by $\mathscr{L}=\Lambda R^{-1}\partial V/\partial x$ represents the strength of the characteristic waves, with its components $\mathscr{L}_i$ being associated to the wave λ_i. It can be shown [9] that

$$\mathscr{L}=\begin{bmatrix} (u-c)\left(\dfrac{\partial p}{\partial x}-\rho c\dfrac{\partial u}{\partial x}\right) \\ u\left(c^2\dfrac{\partial \rho}{\partial x}-\dfrac{\partial p}{\partial x}\right) \\ u\left(\dfrac{\partial v}{\partial x}\right) \\ u\left(\dfrac{\partial w}{\partial x}\right) \\ (u+c)\left(\dfrac{\partial p}{\partial x}+\rho c\dfrac{\partial u}{\partial x}\right) \end{bmatrix} \tag{11}$$

According to the sign of the eigenvalues, the discretization at the boundary has to be done from either inside or outside the domain:

(i) A positive eigenvalue ($\lambda_i>0$) means that the wave is leaving the computational domain and the corresponding value of $\mathscr{L}_i$ must be specified by information inside the domain.
(ii) A negative eigenvalue ($\lambda_i<0$) means that the wave is entering the computational domain and the value of $\mathscr{L}_i$ has to be determined from physical conditions, which characterize the ambient surrounding. The choice of proper conditions is the aim of the proposed improvement for the lateral faces.

In the forthcoming section are detailed the different formulations proposed for the lateral, top and bottom face, respectively.

3.2. Lateral BCs

Three formulations have been investigated on their ability to simulate the dynamics of two co-rotating vortices. In order to explain the choice of the BCs, two-dimensional simulations were performed on two equal vortices placed in the centre of the computational domain (a square box). In the absence of external forces, the two vortices are expected to turn around each other without deviating to the centre of the domain. The challenge for the numerical simulation is to really maintain the vortex system in the centre of the domain: indeed, no physical phenomenon assures this position, and any small grid skewness can lead, in the extreme case, to the exit of the vortices from the computational domain.

While the use of periodic or symmetric BCs at the lateral faces ensures that the vortex system is not deviated, these conditions violate the fact that the total circulation is non-zero. Thus, prescribing such conditions introduces a confinement effect, as it will be shown in Section 5.1, and can lead to the modifications of the dynamics of the merging process. In general, the use of large domains associated with these conditions minimizes these effects. However, for a spatial simulation, these conditions cannot be applied due to their reflective character.

DOI: 10.1002/fld

Three methods to determinate the strength of ingoing waves are investigated:

(i) The first one, proposed by Rudy and Strikwerda [8], imposes a relaxation on the ingoing acoustic characteristic wave to maintain the static pressure in the computational domain at a prescribed value. For the remaining ingoing waves (vorticity or entropy), the strength is simply set to zero. We notice that this may not work well, because the ingoing velocity due to the non-zero circulation propagates information from the outside, and it is in contradiction with zero-strength ingoing wave. At the face $x=x_{\max}$, the characteristic wave strengths are

$$\begin{aligned} &\mathscr{L}_1=\sigma\frac{c}{L}(p-p_{\text{imp}}) \quad \text{if } \lambda_1<0 \\ &\mathscr{L}_i=0 \quad \forall i\in\{2,\ldots,5\} \text{ for which } \lambda_i<0 \end{aligned} \tag{12}$$

where σ is an arbitrary constant, $\sigma\in[0,1]$, p_{imp} indicates a prescribed pressure value and L is a characteristic length of our calculation domain.

(ii) The second formulation is a mixing between the previous BC and an inflow condition. In a first stage, the mean values of the stagnation enthalpy h_{st} and entropy s at this boundary are calculated. These values are then used to determine the incoming flow, but the velocity direction has to be specified to calculate the two remaining unknown wave strengths $\mathscr{L}_3$ and $\mathscr{L}_4$. Usually, the direction is simply assumed to be normal to the boundary. Here, we propose to assume that the incoming flow is irrotational, which means that the vorticity normal to the boundary is assumed to be zero. For the face $x=x_{\max}$ it leads to

- if $u<0$ and $u-c<0$,

$$\frac{\partial u}{\partial y}-\frac{\partial v}{\partial x}=0 \quad \text{and} \quad \frac{\partial u}{\partial z}-\frac{\partial w}{\partial x}=0 \tag{13}$$

These two in Equation (13) allow to calculate the normal derivative of the v and w velocity components

$$\mathscr{L}_3=u\frac{\partial u}{\partial y} \quad \text{and} \quad \mathscr{L}_4=u\frac{\partial u}{\partial z} \tag{14}$$

with the remaining strengths $\mathscr{L}_1$ and $\mathscr{L}_2$ determined using the two following local one-dimensional Inviscid equations (LODI):

$$\frac{\partial h_{\text{st}}}{\partial t}+\frac{1}{\rho(\gamma-1)}\left[-\mathscr{L}_2+\frac{\gamma-1}{2}((1-\mathscr{M})\mathscr{L}_1+(1+\mathscr{M})\mathscr{L}_5)\right]=0 \tag{15}$$

$$\frac{\partial s}{\partial t}+\frac{1}{\rho T(\gamma-1)}\mathscr{L}_2=0 \quad \text{with } s=C_v\log\frac{p}{\rho^\gamma} \tag{16}$$

where $\mathscr{M}=u/c$ and then

$$\mathscr{L}_2=\sigma\rho T(\gamma-1)\frac{c}{L}(s_{\text{imp}}-s) \tag{17}$$

$$\mathscr{L}_1=\frac{2}{(\gamma-1)(1-\mathscr{M})}[\sigma\rho(\gamma-1)(h_{\text{imp}}-h_{\text{st}})+\mathscr{L}_2]-\frac{1+\mathscr{M}}{1-\mathscr{M}}\mathscr{L}_5 \tag{18}$$

DOI: 10.1002/fld

- if $u>0$ and $u-c<0$, a relaxation for the pressure is specified as in the first method (i).

(iii) The third formulation differs from the previous by the calculation of $\mathscr{L}_3$ and $\mathscr{L}_4$. The velocity field in each plane normal to the z-axis is assumed to be written in the form of a superposition of a vortex and a sink.

$$u_s = \sum_{n=0}^{N} \frac{1}{r^n}(a_n \cos(n\theta) + b_n \sin(n\theta))$$
$$v_s = \sum_{n=0}^{N} \frac{1}{r^n}(a_n \sin(n\theta) - b_n \cos(n\theta)) \tag{19}$$

In practice, our numerical experience show that five terms in this summation are enough. For the determination of the coefficients a_n and b_n, we match the velocity field calculated by the NS-equations resolution and the expression (19) in a least-square sense. The matching area consists of a band with a thickness of n points from the boundary. Here, $n=10$ to be enough far away to the vortex dynamics and ensure the $1/r^n$ behaviour. Then the $\mathscr{L}_3$ value is expressed with the previous series as follows:

$$\mathscr{L}_3 = u_s \frac{\partial v_s}{\partial x} \tag{20}$$

In order to determine the strength $\mathscr{L}_4$, we can perform one of the two following methods:

- The x-component of the rotational is assumed to be zero leading to $\mathscr{L}_4 = u\partial u/\partial z$ (all results presented in this paper with this BC were obtained following this method).
- The velocity component w is assumed to relax on a prescribed value.

3.3. Inflow BC

The natural choice of inflow BC for the simulation of spatial vortex dynamics is to impose the vorticity field as inflow condition such as done by Orlandi [3]. The pressure is then calculated by the resolution of the Poisson equation but this cannot be done with a compressible solver. Here, a fundamental difference has to be noticed between incompressible and compressible flow solver since merely information about vorticity is not sufficient to specify the inflow condition. Indeed, like for a subsonic inflow and for a well-posed problem, four quantities must be imposed. The following methods were tested:

(i) all three velocity components and the temperature are specified [9],
(ii) the velocity and temperature are imposed through the characteristic waves [15],
(iii) the stagnation pressure and temperature are specified with the two transverse velocity components.

With the approach (i), temperature and axial velocity are assumed to be uniform and constant. But this choice leads to a vortex breakdown as it will be shown in Section 6.

The second approach (ii) does not ensure that the transverse velocity components remain constant in time. These (even small) intrinsic perturbations cause prematurely merging or unknown level of perturbation, affecting the vortex dynamics.

DOI: 10.1002/fld

The last approach (iii) offers a higher degree of freedom. The stagnation pressure and temperature are calculated at the first time iteration by

$$\begin{aligned} p_{\mathrm{st}} &= p\left(1+\frac{\gamma-1}{2}\mathscr{M}^2\right)^{\gamma/(\gamma-1)} \\ T_{\mathrm{st}} &= T\left(1+\frac{\gamma-1}{2}\mathscr{M}^2\right), \quad \mathscr{M}^2=\frac{u^2+v^2+w^2}{c^2} \end{aligned} \tag{21}$$

The tangential velocity components u and v are prescribed by the vortex strength, while the temperature is assumed to be uniform (equal to $1/\gamma-1$). To determine these two stagnation quantities, a field of pressure and axial velocity have to be chosen. The only constraint is that the pressure should be equal to $1/\gamma$ and the axial velocity must be set to a target value in the outer region of the two vortices. Note that this field can change during the simulation, although the stagnation quantities remain constant.

A Lamb–Oseen vortex model is used in the present numerical study. The corresponding pressure field, denoted by $p_{2\mathrm{D}}$, can be determined analytically. The pressure field used to calculate the stagnation pressure can then be expressed as

$$p=\frac{1}{\gamma}+\alpha\left(p_{2\mathrm{D}}-\frac{1}{\gamma}\right) \tag{22}$$

where α is an arbitrary parameter ($\alpha\in[0,1]$). This parameter allows modifying the deficit of stagnation pressure in the vortex core, which corresponds to various axial velocities in the vortex core. The final pressure field results from an equilibrium between pressure and centrifugal forces, which can be expressed in polar coordinates system such as

$$\frac{\partial p}{\partial r}=\rho\frac{V_\theta^2}{r} \tag{23}$$

The classical method to implement this inflow condition is the following:

(i) Two non-dimensional equations impose that p_{st} and T_{st} remain constant (15) and (16). The components of the entropy wave ($\mathscr{L}_2$) and of one acoustic wave ($\mathscr{L}_1$ or $\mathscr{L}_5$) are determined by setting the two time derivatives to zero.

(ii) These two previous equations correspond to a one-dimensional approximation. As our objective is a three-dimensional simulation, the presence of extra transverse derivatives in Equations (15) and (16) causes a time variation of the two quantities s and h_{st}. To take into account these variations, one can either add a relaxation to their imposed values, or directly impose the prescribed values of the stagnation pressure and stagnation temperature after the last Runge–Kutta step. For an inflow condition at the bottom face, these latter variables are specified

- u,v as transverse velocity components,
- p_{st} and T_{st}.

The axial velocity w (normal to the bottom face) is the only variable that is calculated by the numerical scheme, the other components are deduced from the BC.

This method introduces small perturbations that cannot be controlled and quantified and suffice to perturb the vortices and consequently does not allow the obtention of a time

DOI: 10.1002/fld

converged solution of the vortex system. This converged solution and the addition of a random perturbation constitute the starting point of our simulation of the spatial development of instabilities. The use of a converged solution has for us a particular importance since it uncouples this development of instabilities from the transition phase between the initial solution and the time converged one.

Another method, adopted in this study, consists in taking into account directly the transverse terms in the $\mathscr{L}_i$ calculations. The transverse derivatives can be included in the LODI equations Equations (15) and (16) as

$$\frac{\partial s}{\partial t} - \frac{1}{(\gamma-1)\rho T}\mathscr{L}_2 + \left\{\frac{\partial s}{\partial t}\right\}_{\text{transverse}} = 0 \tag{24}$$

where the last term contains the derivatives with respect to x and y. These terms are simply obtained using

$$\frac{\partial s}{\partial t} = C_v\left(\frac{1}{p}\frac{\partial p}{\partial t} - \frac{\gamma}{\rho}\frac{\partial \rho}{\partial t}\right) \tag{25}$$

To ensure a constant entropy, the strength of the characteristic wave $\mathscr{L}_2$ is given by

$$\mathscr{L}_2 = (\gamma-1)\rho T\left\{\frac{\partial s}{\partial t}\right\}_{\text{transverse}} \tag{26}$$

With this choice, the temporal integration of the NS equations gives a constant entropy without further treatments. The same treatment is applied to the stagnation enthalpy as

$$\frac{\partial h_{\text{st}}}{\partial t} = \frac{\gamma}{\gamma-1}\left(\frac{1}{\rho}\frac{\partial p}{\partial t} - \frac{p}{\rho^2}\frac{\partial \rho}{\partial t}\right) + u\frac{\partial u}{\partial t} + v\frac{\partial v}{\partial t} + w\frac{\partial w}{\partial t} \tag{27}$$

A formulation for $\mathscr{L}_1$ or $\mathscr{L}_5$ can now be found with $\partial h_{\text{st}}/\partial t = 0$ exactly respected.

3.4. Outflow BC

Since no inflow is expected through the top face, a simple relaxation is imposed on the pressure. Nevertheless, since the pressure decreases in the vortex core region, this relaxation must vanish in this area. If the relaxation procedure is preserved in the vortex core, this acts like a pressure wave travelling in the vortex, potentially leading to the destruction of the vortex structure (vortex bursting [16]).

A blending function is thus introduced to reduce the relaxation factor σ (Equation (12)) smoothly to zero at the location of maximum vorticity defining the vortex centre. The blending function is defined by

$$\sigma = \sigma^*\left(1 - \min\left[1, \max\left(0, \frac{\omega-\omega_l}{\omega_l}\right)\right]\right), \quad \omega_l = \varepsilon\omega_{\max} \tag{28}$$

where $\omega_{\max}$ represents the maximum of the vorticity at the top face. σ^* and ε are arbitrary parameters, and we propose to set $\sigma^* \in [0.0, 1.0]$ and $\varepsilon \approx 0.001$. The value of σ^* permits to recover the prescribed value of the relaxation parameter as suggested by Rudy and Strikwerda (Equation (12)). The second value influences the size of the region around the point of maximal vorticity a lower

DOI: 10.1002/fld

value leads to larger size. The proposed value is obtained by the study of an isolated vortex as the merging process reduces to one vortex, and the relaxation has to be inactive in those regions where the pressure is lower than 1% of the free stream value.

3.5. Outflow BCs: Giles approach

The outflow BC at the top plane based on the Poinsot–Lele approach, is perfectly non-reflective only for plane waves, which have a propagation direction aligned to the boundary normal. For other wave, this boundary treatment leads to unphysical reflecting waves. Giles proposed [5, 17] a general theory to obtain a non-reflecting condition for the two-dimensional linearized Euler equations. He discussed the different formulations depending on the steadiness or unsteadiness of the flow. In the following, the general theory is briefly presented in the case of unsteady flow (as in our final application).

3.5.1. Basic formulation. The starting point for the Giles analysis are the linearized Euler equations for a Cartesian coordinates system about an average or reference primitive state vector $\bar{V} = (\bar{\rho}, \bar{u}, \bar{v}, \bar{w}, \bar{p})$. For the perturbed state variable vector V around the state $\bar{V}$, the equations are

$$\frac{\partial V}{\partial t} + A\frac{\partial V}{\partial x} + B\frac{\partial V}{\partial y} + C\frac{\partial V}{\partial z} = 0 \tag{29}$$

The Jacobian matrices A, B, C are constant and calculated from the average state. To separate waves into incoming and outgoing ones, the perturbed state is decomposed into a Fourier series

$$V(x, y, z, t) = \sum_{\ell=-\infty}^{\infty} v_\ell \mathrm{e}^{\mathrm{i}(-\omega_\ell t + k_\ell x + l_\ell y + m_\ell z)} \tag{30}$$

Introducing this relation into Equation (29) gives a dispersion relation, which relates the wave numbers k, l, m to the frequency ω over an homogeneous fifth-order polynomial expression.

To formulate a condition for a non-reflecting axial boundary, we decompose the particular mode V_ℓ into the sum of its eigenfunctions

$$V_\ell = \left(\sum_{n=1}^{5} a_n \mathfrak{q}_n^R \mathrm{e}^{\mathrm{i}m_n z} \right) \mathrm{e}^{\mathrm{i}(-\omega t + kx + ly)} \tag{31}$$

where m_n represents one of the five eigenvalues corresponding to acoustic, entropic or rotational modes and $\mathfrak{q}_n^{\mathrm{R}}$ is the corresponding right eigenvector.

Reflections at the boundary can now be prevented by specifying $a_n = 0$ for each n in Equation (31) corresponding to an incoming wave.

The latter condition can be expressed by introducing the left eigenvector $\mathfrak{q}_n^{\mathrm{L}}$ corresponding to the same incoming wave by

$$\mathfrak{q}_n^{\mathrm{L}} V_\ell = 0 \quad \text{with } n \text{ the incoming wave index} \tag{32}$$

The dispersion relation shows that m_n/ω and $\mathfrak{q}_n^{\mathrm{L}}$ depend on $\lambda = k/\omega$ and $\mu = l/\omega$. To obtain a local BC, the left eigenvector $\mathfrak{q}_n^{\mathrm{L}}$ is expanded into a Taylor series as function of λ and μ. The following second-order approximation is

$$\mathfrak{q}_n^{\mathrm{L}}(\lambda, \mu) \approx \mathfrak{q}_n^{\mathrm{L}}(0,0) + \lambda \frac{\partial \mathfrak{q}_n^{\mathrm{L}}}{\partial \lambda}(0,0) + \mu \frac{\partial \mathfrak{q}_n^{\mathrm{L}}}{\partial \mu}(0,0) + O(\lambda^2, \mu^2, \mu\lambda) \tag{33}$$

DOI: 10.1002/fld

Throughout this approximation, the non-reflecting condition (Equation (32)) leads to the following evolution equation:

$$\mathfrak{q}_n^{\mathrm{L}}(0,0)\frac{\partial V_\ell}{\partial t}=\frac{\partial \mathfrak{q}_n^{\mathrm{L}}}{\partial \lambda}(0,0)\frac{\partial V_\ell}{\partial x}+\frac{\partial \mathfrak{q}_n^{\mathrm{L}}}{\partial \mu}(0,0)\frac{\partial V_\ell}{\partial y} \tag{34}$$

This corresponds to a local BC, but is only approximately of non-reflecting nature as it potentially generates large reflections of outgoing waves for which k or l are large.

After some algebraic manipulations, the previous Equation (34) can be expressed in terms of the characteristic variables $\mathscr{W}$, and reads for the top face

$$\frac{\partial \mathscr{W}_5}{\partial t}+(0,w,0,0,u)\frac{\partial \mathscr{W}}{\partial x}+(0,0,w,0,v)\frac{\partial \mathscr{W}}{\partial y}=0 \tag{35}$$

when only the acoustic wave associated with $w-c$ enters in the computational domain, and

$$\begin{aligned}
\frac{\partial \mathscr{W}_1}{\partial t}+(u,0,0,0,0)\frac{\partial \mathscr{W}}{\partial x}+(v,0,0,0,0)\frac{\partial \mathscr{W}}{\partial y}&=0\\
\frac{\partial \mathscr{W}_2}{\partial t}+\left(0,u,0,\frac{1}{2}(w+c),\frac{1}{2}(c-w)\right)\frac{\partial \mathscr{W}}{\partial x}+(0,v,0,0,0)\frac{\partial \mathscr{W}}{\partial y}&=0\\
\frac{\partial \mathscr{W}_3}{\partial t}+(0,0,u,0,0)\frac{\partial \mathscr{W}}{\partial x}+\left(0,0,v,\frac{1}{2}(w+c),\frac{1}{2}(c-w)\right)\frac{\partial \mathscr{W}}{\partial y}&=0\\
\frac{\partial \mathscr{W}_5}{\partial t}+\left(0,\frac{1}{2}(w+c),0,0,u\right)\frac{\partial \mathscr{W}}{\partial x}+\left(0,0,\frac{1}{2}(w+c),0,v\right)\frac{\partial \mathscr{W}}{\partial y}&=0
\end{aligned} \tag{36}$$

when the waves associated with $w-c$ and w are incoming waves.

3.5.2. Present modifications. In the original Giles paper [5], the state vector $\bar{V}$ is supposed to be known by a preliminary steady simulation or by an analytical formulation. For our final application, this reference state is determined by a sliding time average. This variation in time of the reference state enables to reduce the strength of outgoing waves by a continuous adaptation of this reference state to the real flow, and to limit the wavenumber of these perturbations. This feature is important in the context of the approximation done for the unsteady Giles condition.

However, this BC does not assure that the average pressure, as example, remains close to the prescribed value. The passage of a perturbation might cause a drift away from this, and one has to simulate the effects of a large undisturbed atmosphere surrounding the computational domain. To do that, the relaxation process proposed in Equation (12) is imposed on the reference state.

As explained by Bruneau and Creuse [18], the strength of a characteristic wave is in fact decomposed into two parts: one is related to the evolution of the reference state and the other one is due to the perturbations around the reference state. This second strength is determined by the non-reflecting BCs (Equations (35) or (36)).

To evaluate the first part, the same sliding average in time is not only applied to the boundary point but also to the first two interior points. These three points allow the determination of the outgoing waves strength, and then the incoming waves strength can be determined by specifying

DOI: 10.1002/fld

a physical behaviour. For the top face, the same relaxation process is applied to the reference pressure as described in Section 3.4.

It can be noticed that all BCs presented in Sections 3.2 or 3.4 could be used for the sliding time average state.

3.6. Corner treatment

To conclude with the BCs, a simple specific corner treatment is presented. A corner point of the computational domain in finite difference discretization constitutes a singular point in terms of BC specification. Two classic treatments can be used:

(i) Extrapolation method: the state vector is calculated from an interpolation between the two neighbouring border points. In our experiment, this leads to spurious pressure waves, which might propagate into the domain and causes the divergence of the calculation and Lele filter cannot overcome this drawback.
(ii) Segregation method: the corner point is associated only to one border, the BC applied at this border takes into account this point, while the BC of the other side is simply ignored. This method has two drawbacks: the first one lies in a di-symmetrization (one condition is assumed to predominate the other one) and secondly, low-level perturbation waves are generated, and must be damped by the application of the Lele filter [13] near the border, or a sponge-layer region.

A different treatment for these corner points is proposed and tested here. It is assumed that the direction of the waves coming at the corner is given by **n** (see Figure 2), and the two points designed by a *new discretization point* (crosses points) are used. The lateral BCs presented in Section (3.2) is employed in the $(\mathbf{n}, \mathbf{t})$ frame. For the sake of simplicity, the two-dimensional case is the only one presented here. To discretize the terms at the corner, the following procedure is used:

(i) The NS equations are discretized with the same finite difference scheme as an interior point. The compact schemes are upwinded at the boundary as proposed in [19]. Only the neighbouring boundary points are used.
(ii) The discretized equations are projected on the $(\mathbf{n}, \mathbf{t})$ frame, the term corresponding to the component in the **n**-direction is subtracted to the discretized equations.

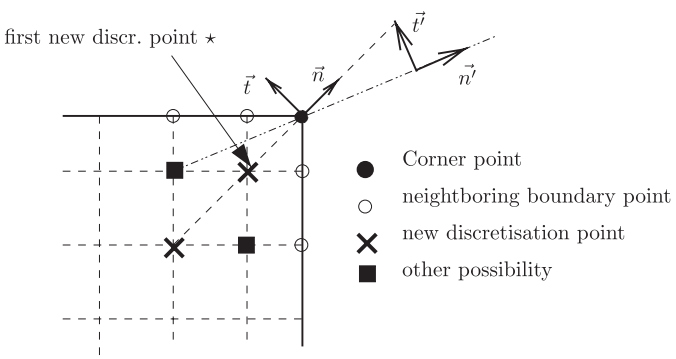

Figure 2. Corner discretization.

DOI: 10.1002/fld

(iii) A new formulation for the **n**-component is added to the previous equations. This term results in the NS-characteristic BC (NSCBC) equations for the **n**-direction, and the new discretization points are used to compute the strength of the outgoing characteristic waves $\mathscr{L}_i$. For the present study, a second-order accuracy formula is used to compute these $\mathscr{L}_i$.

For example, the zero-rotational condition in the $(\mathbf{n}, \mathbf{t})$ frame is

$$\frac{\partial(\mathbf{V}\cdot\mathbf{n})}{\partial t} - \frac{\partial(\mathbf{V}\cdot\mathbf{t})}{\partial n} = 0 \tag{37}$$

For certain cases, we observe the development of numerical wiggles near the corner points. These difficulties are linked to the fact that, physically, for a single vortex placed at the centre of the computational domain discretized by a symmetric mesh, the velocity must be in the **t**-direction. This corresponds to a zero **n**-component, which poses many problems for the NSCBC conditions as they constitute an ill-conditioned problem. Since the velocity in the **n**-direction is very small, the nature of the BC can switch at each time step from an inflow condition to an outflow ones.

For this case, we propose using the *other option* points, symbolized by squares in Figure 2, that simply break the symmetry and lead to a non-zero velocity component in the new resulting $\mathbf{n}'$-direction. The NSCBC conditions are now expressed in the $(\mathbf{n}', \mathbf{t}')$ frame, using a first-order formula for the $\mathscr{L}_i$ calculation.

With our application, there is no influence on the choice of this *other discretization* points. The choice is left to the user.

In practice, to switch from the first corner discretization ($(\mathbf{n}, \mathbf{t})$ frame) to the ($(\mathbf{n}', \mathbf{t}')$ frame), the velocity direction is tested during the calculation at the point denoted with a star ($\star$) in Figure 2:

$$\begin{aligned} \text{if } \frac{\mathbf{V}\cdot\mathbf{n}}{\|\mathbf{V}\|} > 0.001 &\Rightarrow \text{use } (\mathbf{n}, \mathbf{t}) \\ \text{else} &\Rightarrow \text{use } (\mathbf{n}', \mathbf{t}') \end{aligned} \tag{38}$$

The gain of corner point treatment is discussed in Section 5.1.

4. NUMERICAL APPROXIMATION

In this section we present the specific numerical treatment used for the spatial simulation of a two co-rotating vortices system.

4.1. Definition of the sponge layer

Although our BCs are non-reflective, some spurious waves could be generated and a sponge layer must be added to reduce the amplitude of the outgoing waves in the hope to reduce the reflecting waves. For the direct numerical simulation of jet flows, sponge layers are widely used (see for example [20, 21]). They offer the possibility to dump outgoing waves, thus reducing significantly unphysical reflections, by using a second-order filter [22]. Inside these sponge layers, a source term can be added to the NS equations to relax the state vector to a known reference state (analytical solution or undisturbed flow).

In our case, no sponge layer is set at the top face since the resulting vortex from the merging process across this boundary is unknown. Adding a second-order filter at this face produces perturbations upstream from this boundary.

DOI: 10.1002/fld

At the lateral faces, a sponge layer is added to the computational domain, in which a second-order filter can be applied on several points close to the border (here, no more than five points). The state vector U is filtered in this zone to give a state U^{f}, for the x-downwind side defined by

$$U^{\mathrm{f}}_{i,j,k} = U_{i,j,k} - \kappa \left(\frac{x_{i,j,k} - x_{\mathrm{sponge}}}{x_{i_{\mathrm{m}},j,k} - x_{\mathrm{sponge}}} \right)^{1.5} \times \left[\frac{3}{2} U_{i,j,k} - \frac{1}{4} \left(U_{i+1,j,k} + U_{i-1,j,k} + U_{i,j+1,k} + U_{i,j-1,k} + U_{i,j,k+1} + U_{i,j,k-1} \right) \right] \quad (39)$$

where i_{m} is the maximum value of the i index and x_{sponge} is the abscissa of the sponge layer beginning. κ is an arbitrary parameter, which controls the filtering intensity. A value of 0.01 is used in our computations. For the spatial merging study, x_{sponge} is equal to the abscissa of the third point from the considered x-downwind side.

Moreover, with the lateral BC exposed in Section 3.2, the axial velocity is not prescribed and a drift from the initial value was observed. To suppress this phenomenon, a relaxation process is incorporated in the equation of the axial velocity component. We have chosen to apply this process on the averaged axial velocity $\bar{w}$, contrary to the classical formulation, where it is applied directly on the instantaneous velocity. This choice has been motivated by the reduction of the reflecting waves strengths coming from this relaxation. Physically, this relaxation means that a perturbation can create a drift from the prescribed velocity when leaving the computational domain, but the mean velocity should remain close and relax towards it. A source term is added on the right-hand side (Equation (1)) of the momentum equation in the axial direction such as

$$\frac{\partial \rho w}{\partial t} = \mathrm{RHS} + \kappa_{\mathrm{s}} (\bar{\rho}\bar{w} - \bar{\rho} w_{\mathrm{in}}) \quad (40)$$

where $\bar{\phi}$ designs a sliding average in time of the variable ϕ, w_{in} represents the freestream axial velocity and κ_{s} a free parameter to adjust the relaxation strength. We found that $\kappa_{\mathrm{s}} = 0.05$ appears to be sufficient.

4.2. Selective artificial dissipation

It is well known that centered finite difference schemes are subject to numerical instabilities when spurious solutions from the discrete problem are excited by the approximations caused by the BCs, grid stretching or under-resolved flow gradients. This type of high wavenumber instability may be overcome by either adding an artificial dissipation through upwinding, by adding explicit damping terms, or by filtering the solution. We have chosen to follow the approach of Tam and Webb [23] and Barone [19] by adding a selective damping term to the equations. Requirements for the damping term include: (1) it must be strongly limited for well-resolved spatial wavenumbers, (2) error estimation from the added dissipative terms must be available (3) the additional error from the damping operator should be linked to the ratio between the flow and mesh scales instead of only to the grid spacing. The suitable artificial dissipation operator is an approximation of the sixth derivative scaled by the fifth power of the grid spacing:

$$D_x = \gamma (\Delta x)^5 \frac{\partial^6 U}{\partial x^6} \quad (41)$$

DOI: 10.1002/fld

The sixth derivative is chosen due to the k^6 scaling in the spectral space, where k is the spatial wavenumber. The damping is strongly restricted to the high wavenumber of the spectrum due to this functional form.

Given that a compact approximation to the sixth derivative will more faithfully represent the k^6 behaviour in spectral space than an explicit scheme, we determine implicitly D_ξ by using the finite difference approximation for the sixth derivative in the computational space:

$$\left.\frac{\partial^6 U}{\partial \xi^6}\right|_{i-1} + \alpha \left.\frac{\partial^6 U}{\partial \xi^6}\right|_{i} + \left.\frac{\partial^6 U}{\partial \xi^6}\right|_{i+1} = a_0 U_i + \sum_{l=1}^{3} a_l (U_{i+l} + U_{i-l}) \tag{42}$$

with

$$\alpha = 3, \quad a_0 = 80, \quad a_1 = -60, \quad a_2 = 24, \quad a_3 = -4 \tag{43}$$

For the two first interior points, the artificial dissipation must be modified, using a second- and a fourth-order derivative, respectively.

$$\left.\frac{\partial^2 U}{\partial \xi^2}\right|_{i-1} + 10 \left.\frac{\partial^2 U}{\partial \xi^2}\right|_{i} + \left.\frac{\partial^2 U}{\partial \xi^2}\right|_{i+1} = 2U_i - (U_{i+1} + U_{i-1}) \tag{44}$$

$$\left.\frac{\partial^4 U}{\partial \xi^4}\right|_{i-1} + 5 \left.\frac{\partial^4 U}{\partial \xi^4}\right|_{i} + \left.\frac{\partial^4 U}{\partial \xi^4}\right|_{i+1} = 36U_i - 24(U_{i+1} + U_{i-1}) + 6(U_{i+2} + U_{i-2}) \tag{45}$$

For the boundary points, the artificial dissipation is set to zero.

The artificial dissipation D_ξ is first computed in the computational space and then expressed in the physical space using the relation

$$D_x = \frac{1}{x_\xi} D_\xi \tag{46}$$

In order to compute the metric term x_ξ, Lele's compact formulation [13] is used as approximation of the first-order derivative. For our computations, the value of the parameter γ (in Equation (41)), which controls the strength of the dissipation is set between 0.001 and 0.006.

5. NUMERICAL TOOLS VALIDATION

5.1. Influence of the lateral BC

To see the influence of the lateral BCs, it has been chosen to simulate a co-rotating vortex system in a bi-dimensional square domain. The vortex dynamics is governed by a rotational motion of the vortex system due to the induced velocity of one vortex on its neighbour, while the vortex system does not reach the critical value $(a/d)_c \sim 0.22$ [24] between the vortex core size a (dispersion radius) and the separation distance d. For all the tests presented in this section the initial characteristic parameter is $(a/d)_0 = 0.1$ and the Reynolds number is $Re_\Gamma = 10^6$ (where Γ is the circulation of one vortex). As the viscosity effects are very slight, the vortex core size increases very slowly. There are no external forces to push one vortex towards the other, thus the separation distance between the two vortices does not change. The ratio a/d grows very slowly, and a large number of turnover could be performed before this ratio reaches its critical value $(a/d)_c$.

DOI: 10.1002/fld

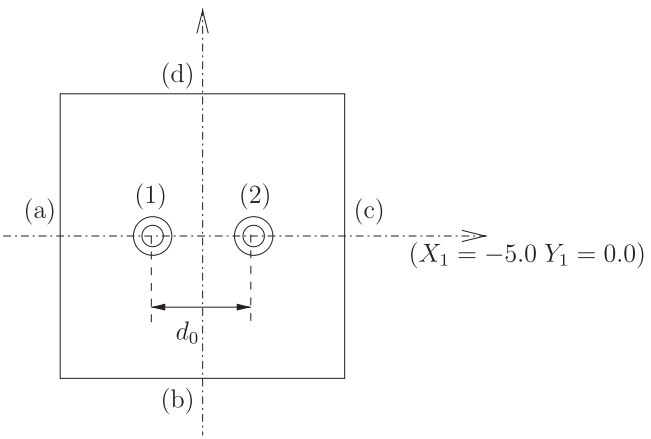

Figure 3. Computational domain and boundary specification.

The vortex system is initially placed on the computational domain centre (Figure 3). Each vortex is initially defined with a Lamb–Oseen formulation. The vorticity field is described by

$$\omega_1 = \frac{\beta\Gamma}{\pi r_c^2}\exp(-\beta(r/r_c)^2), \quad r = \sqrt{(X-X_1)^2+(Y-Y_1)^2} \tag{47}$$

where (X_i, Y_i) are the coordinates of one vortex centre, $\beta = 1.12^2$, and r_c its core radius defined as the radius where the azimuthal velocity is maximum. Note that the circulation is related to the maximum azimuthal velocity V_0 by $\Gamma = 2\pi\alpha r_c V_0$ with $\alpha = 1.4$. For this specific study, V_0 is set to 0.4 and the separation distance d_0 between the two vortices is equal to $10r_c$. The domain considered is a square of length $L = 31r_c$. These choices of domain length and azimuthal maximum velocity are intentionally chosen to be defavourable for the treatment of BCs. Indeed, the induced velocity by the vortex system at the boundaries is not negligible, and approximatively equals to $\sim 9.3\% V_0$. When considering the final spatial simulation, the transverse domain length cannot be too large for computational cost reasons. To test our BCs in preparation of this application, the size of the computational domain is relatively small, and the mesh is stretched towards the border in order to limit the total number of grid points. If one vortex enters in the stretched region, the mesh is too coarse to discretize properly the vortex flow and leads to an unacceptable numerical solution. As there are no external forces, the vortex system should remain in the centre of the domain where the grid resolution is fine.

The influence of the lateral BCs is analysed regarding their capacity to respect the property to maintain the vortex system in the domain centre, and to respect the turnover period of the vortex system, defined by $T = 2\pi^2 d_0^2/\Gamma$. Five different BCs have been tested:

(i) periodic,
(ii) symmetric,
(iii) non-reflective (Section 3.2, (i)),
(iv) inflow/outflow BC associated with a zero-rotational condition (Section 3.2, (ii)),
(v) inflow/outflow BC associated with the use of an expansion (Section 3.2, (iii)).

DOI: 10.1002/fld

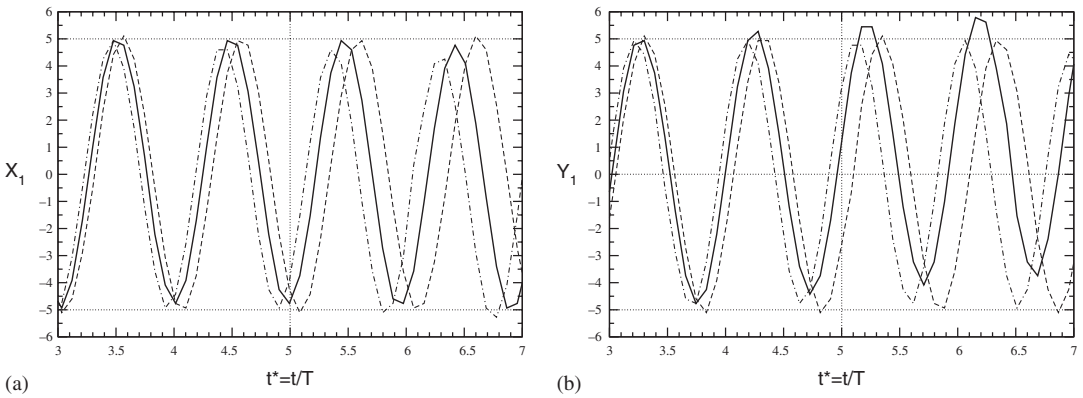

Figure 4. Horizontal (a) and vertical (b) position of one vortex centre as function to the normalized time for different lateral boundary conditions. Dashed line: symmetric, solid line: zero rotational and dashed-dot line: non-reflective.

It should be noticed that the two first conditions are classically used for vortex dynamics simulation in conjunction with large domains to reduce their effects. The use of such domain is acceptable for temporal simulation, but leads to huge number of points for spatial simulations.

All calculations were performed until ~ 11 turnover periods of the vortex system. Figure 4 represents the vortex centre position of one vortex as function to the normalized time $t^* = t/T$. The first analysis focuses around the time $t^* = 5$, as the effects of the lateral BC are not visible before. This value of five turnover periods corresponds to the maximum turnover number observed in our final application. The results with periodic conditions are not plotted on this figure as they are identical to the ones with symmetric conditions. The vortex centre is localized by the vorticity extremum. At the time $t^* = 5$, the vortex should be at its initial position ($X_1 = -5$; $Y_1 = 0$), all the results differ from this position:

- the use of symmetric condition (ii) leads to slight time advanced solution,
- with the non-reflective condition (iii) the solution is slightly delayed,
- with the condition (iv) the solution is in good agreement for the horizontal position and the closer for the vertical position,
- for the condition (v), the vortex system is completely shifted from the domain centre but the results are in good agreement with the physics as far as the turnover period of the vortex system is concerned (see Figure 5(a)).

This discrepancy of the vortex position increases with time, for example at $t^* = 10T$ with the symmetric BC the time advanced solution reaches one half turnover period.

The second point under interest lies in the capacity to maintain the vortex system in the centre of the calculation domain. All NSCBC show the same drawback that the vortex system deviates from the centre, but the magnitude differs with respect to the type of NSCBC. Indeed, with the conditions (iv) this drift increases slowly in time, while it is more sudden and pronounced with the condition (iii), and seems to evolve linearly with the conditions (v) (see Figure 5(b)).

An observation of the streamlines (Figure 6) confirm the previous behaviours. The confinement effect is well depicted with the symmetric or periodic BCs, and the use of such conditions for vortex flow requires large domain to minimize this effect.

DOI: 10.1002/fld

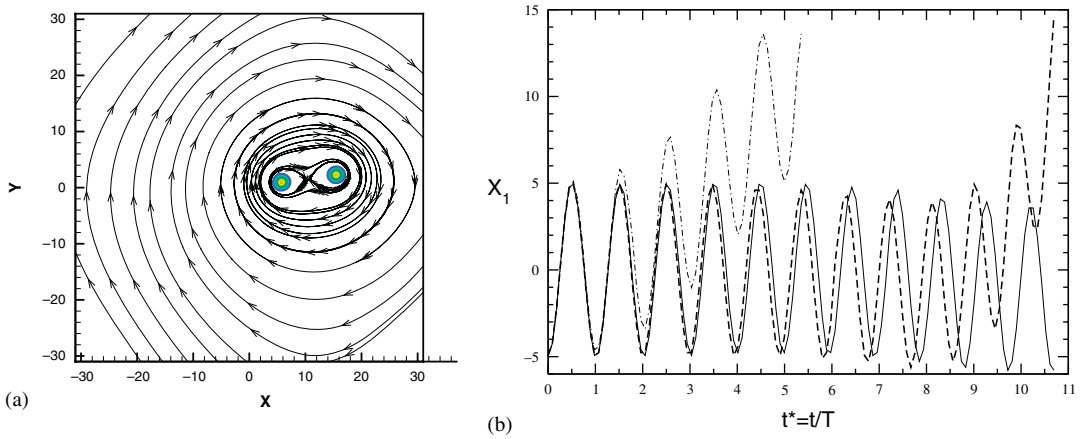

Figure 5. (a) Qualitative analysis of the streamlines at the normalized time $t^* = t/T = 5$ for the series expansion boundary conditions and (b) horizontal position of one vortex centre for different lateral boundary conditions. Dashed line: non-reflective, solid line: zero rotational and dashed-dot line: series expansion.

As regards the BCs based on the NSCBC approach, the streamlines show the inflow and the outflow at the border. This illustrates the difficulty to build such BCs that must be

- non-reflecting for perturbations,
- able to predict correctly the flow coming from the exterior of the domain.

The purely non-reflecting BC (iii) fails to fulfil this second point. Only the two new approaches (iv) and (v) are able to satisfy the two properties. However, some spurious waves propagating into the domain or skewness in the inflow rate lead to a displacement of the vortex system.

To damp these spurious waves a sponge or buffer layer with a filter (see Section 4.1 for example) can be used. The skewness in the inflow rate has been observed principally in the neighbourhood of the corners, since the direction of the flow velocity is not well predicted at this point. This behaviour should be improved by the use of the corner treatment (Section 3.6). Calculations performed with sponge layer and corner treatment are shown on Figure 7. For condition (iii), the influence of both sponge layer or corner treatment are studied separately. It appears clearly that the use of a buffer layer is not sufficient in this case, but the additional corner treatment allows to minimize the deviation of the vortex system for long calculation time. However, as in the case of BCs with series expansion (v), the results show the slow time deviation of the vortex position. The use of the BCs with series expansion (v) without numerical treatment leads to a deviation of the vortex system starting from the beginning of the simulation (Figure 5(b)). With the buffer layer and corner treatment this deviation begins latter and is damped. While with the zero-rotational BCs (iv) and additional numerical treatments, the results are very similar to the one without numerical treatments (Figure 5(b)).

These results show the difficulty to correctly take into account the flow induced by the vortex system at the borders, linked to the non-zero circulation of the co-rotating vortex system. For three-dimensional spatial development of a co-rotating vortex system, conditions (iv) or (v) (with a buffer

DOI: 10.1002/fld

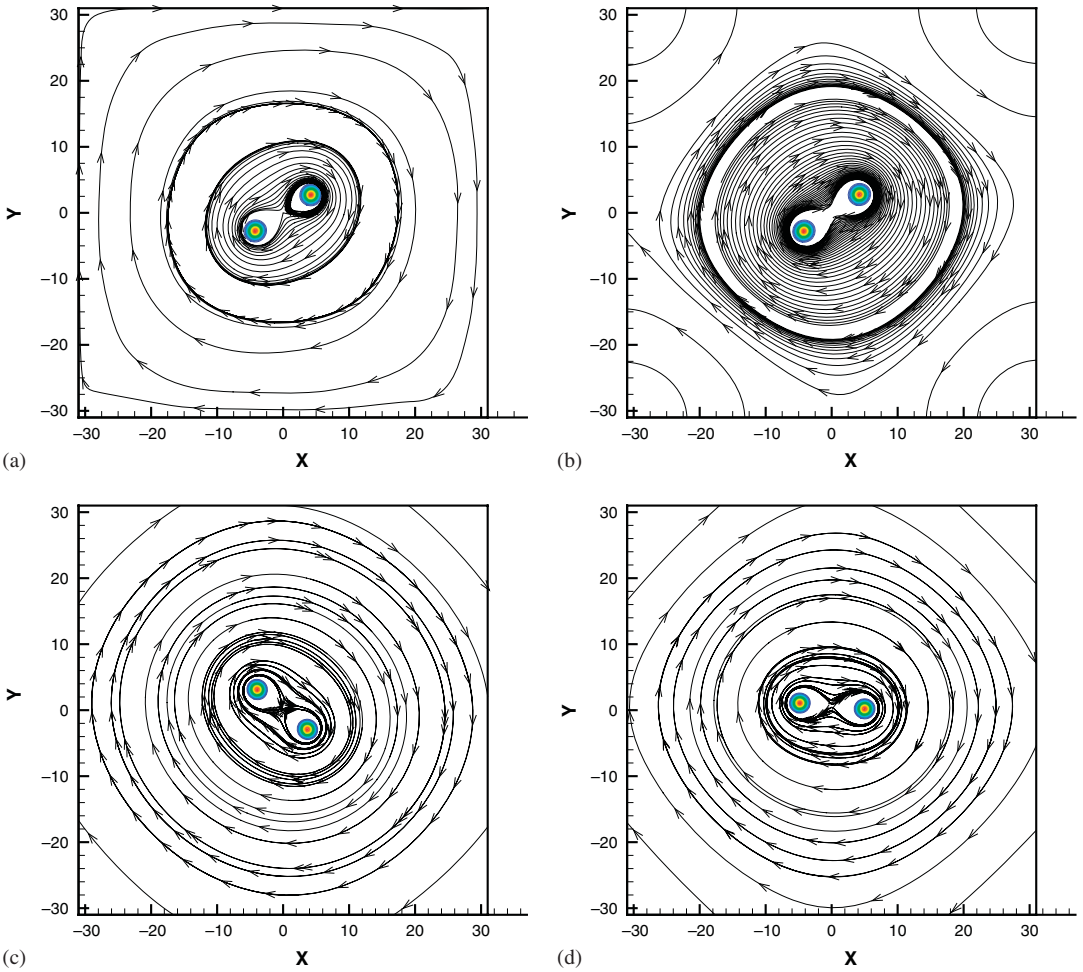

Figure 6. Qualitative analysis of the different lateral boundary conditions, illustrated by the streamlines at the normalized time $t^* = t/T = 5$: (a) symmetric; (b) periodic; (c) non-reflective; and (d) zero rotational.

layer) seem to be the best choice, as they respect the physics more. However, condition (v) requires the determination of expansion coefficients (Section 3.2), which increases the computational cost and so will not be used in our final application.

5.2. *Influence of the inflow BC*

To test the inflow BC, three-dimensional simulations of an isolated vortex are considered. The computational domain is defined by a box of $40r_c$ in the transverse direction and $100r_c$ in the axial one. A Lamb–Oseen vortex model is used to determine the transverse velocity values for the inflow BC. The Reynolds number based on the vortex circulation is $Re_\Gamma = 10^4$, as employed for the final application.

DOI: 10.1002/fld

The objective of these simulations is to show the influence of the stagnation pressure and temperature on the development of an isolated vortex. The results are analysed once a statistical time converged solution has been obtained. The total temperature remains identical in all cases, while the parameter α introduced in Equation (22) varies. Five values have been tested: $\alpha = 0.0, 0.1, 0.2, 0.4, 0.6$. Note that with an increased value of α, the deficit of the stagnation pressure in the vortex core rises.

In Figure 8, the axial evolution of the axial velocity in the vortex core is presented. For a small value of α, the axial velocity decreases linearly. This is due to the increase of the minimum pressure

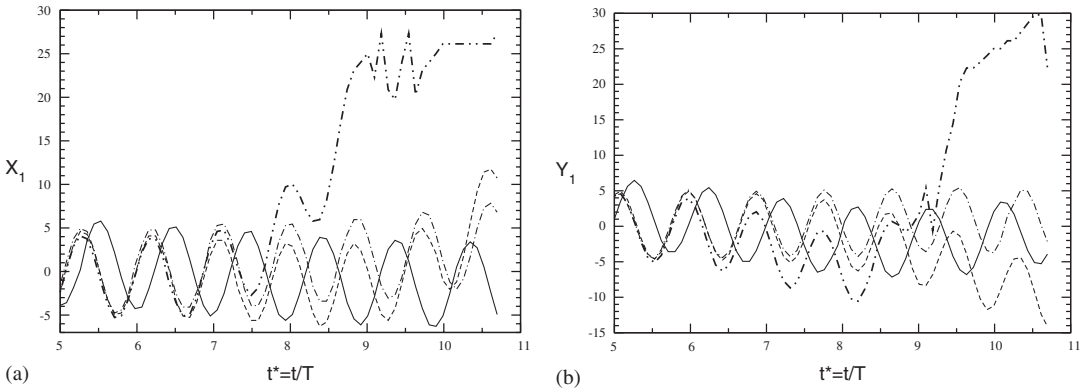

Figure 7. (a) Horizontal and (b) vertical position of one vortex centre as function to the normalized time, for different lateral boundary conditions coupled to a numerical treatment at the boundaries. Dashed line: non-reflective with corner treatment, dashed-dot–dot line: non-reflective without corner treatment, solid line: inflow/outflow with zero rotational, dashed-dot line: inflow/outflow with series expansion.

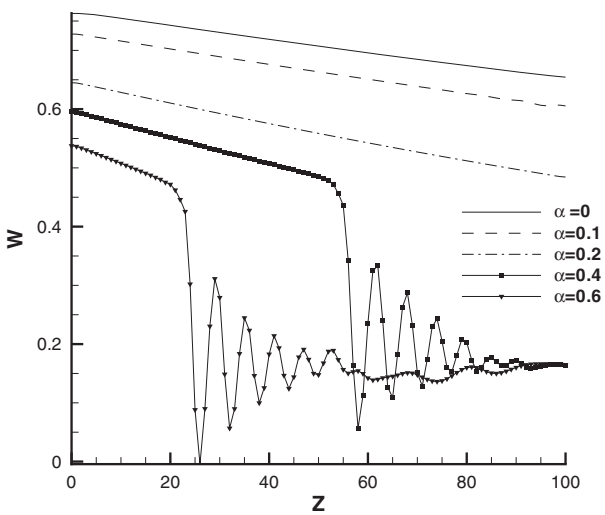

Figure 8. Influence of α: axial velocity in the vortex core function to the axial direction z.

DOI: 10.1002/fld

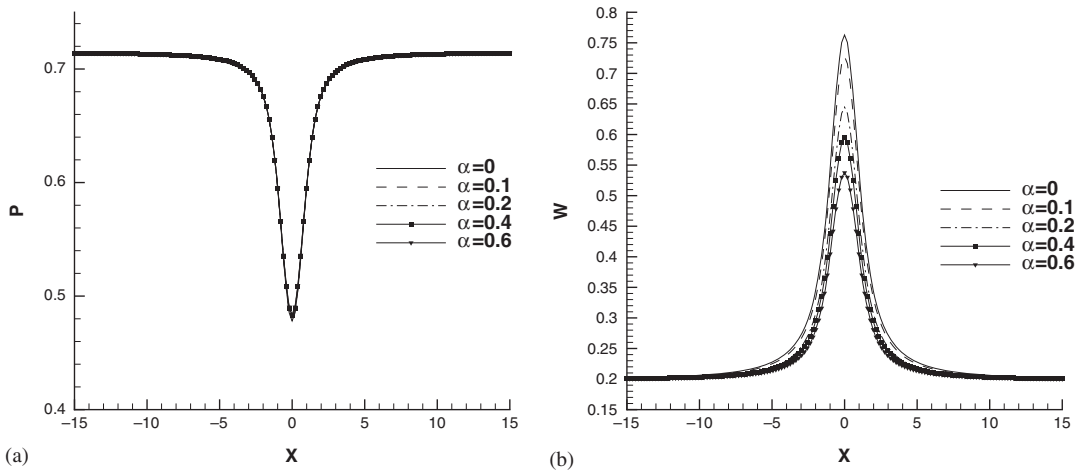

Figure 9. Influence of α parameter at the inflow boundary $z=0$: (a) pressure distribution in the vortex and (b) axial velocity distribution through the vortex.

in the vortex core, which is correlated to the diminishing of the transverse velocity components caused by the diffusion. Increasing the value of α leads to a decrease of the axial velocity level. For the values 0.4 and 0.6, a large decrease of the axial velocity is observed at a particular downstream distance, and this distance between the inflow face and the breaking point is inversely proportional to α.

Figure 9(a) presents the pressure distribution through the vortex in the bottom plane. This field is not modified by the variation of the α-value, which can be explained by the fact that the pressure distribution derives directly from an equilibrium between the pressure and the centrifugal forces (Equation (23)). A modification of the stagnation pressure induces only a variation of the axial velocity. In particular, if the value of α increases, the axial velocity peak decreases (Figure 9(b)) at the bottom face. Moreover, due to the viscosity effects, this velocity peak continues to decrease in the downstream distance. To characterize the flow, we can use the swirl parameter S, defined as the ratio between the azimuthal velocity peak and axial one. Billant *et al.* [25] have shown that for swirling jets, the vortex breakdown phenomenon appears when the swirl parameter reaches a critical value of $S_c=1.4\pm0.18$. For the two cases in which the vortex breakdown phenomenon occurs here, $\alpha=0.4$ and $\alpha=0.6$, the swirl number evaluated at the axial position of $z=20$ and $z=54$, respectively, is in good agreement with the experimental critical value.

Since this strong physical phenomenon can disturb the spatial simulation of the merging process, $\alpha=0$ will be used for our final simulation. This means that only 'jet-vortex' are under consideration. This limitation is not too restrictive since a wake vortex generated by a vorticity wake roll-up shows such characteristics in its first stage of formation.

5.3. Influence of the outflow condition

In order to validate the non-reflective character of the outflow BC, two-dimensional simulations of the convection of a Lamb–Oseen vortex through the boundary were performed. This test case is more difficult for the BC than for the final case, because the vortex axis is parallel and not

DOI: 10.1002/fld

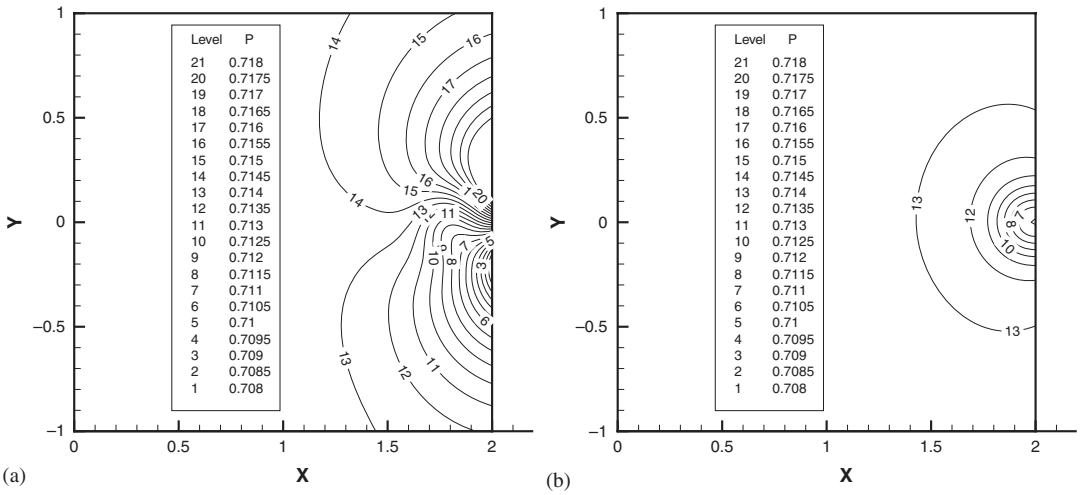

Figure 10. Line isopressure values: (a) non-reflective condition and (b) Giles condition.

perpendicular to the exit plane. However, as some perturbations will be injected for the final simulation, the vortex axis might become inclined, or the vortex might become unstructured and the situation is not too far from the simplified one proposed here.

Two BCs are investigated, the classical non-reflective one and the proposed one (Section 3.5) based on Giles approach. The non-dimensional convection velocity is set to 0.2. The iso-pressure lines are used to discuss the efficiency of the BC. The vortex travels through the boundary without generating unphysical reflections for the Giles conditions unlike the classical non-reflecting condition as seen in Figure 10. More precisely, the time evolution of the maximum of vorticity and pressure are presented. Both quantities are made non-dimensional by their initial values. The wave reflection phenomenon obtained with the classical non-reflecting condition is brought out by the increase of the maximum value of pressure or vorticity as the vortex leaves the computational domain (Figure 11). It must be noticed that the non-reflecting condition generates vorticity, which could be dramatic for vortex simulation. For the final simulation, Giles condition will be used at the top face.

5.4. Influence of the artificial dissipation

Two aspects of the selective artificial dissipation proposed in Section 4.2 will be tested here:

(i) overestimation of viscosity,
(ii) damping of perturbations.

For the first aspect (i), we compare the time evolution of the radius of an isolated Lamb–Oseen vortex computed by a two-dimensional simulation. The core radius r_c increases by diffusion according to

$$r_c(t) = \sqrt{4\nu\beta t + r_{c0}^2} \tag{48}$$

DOI: 10.1002/fld

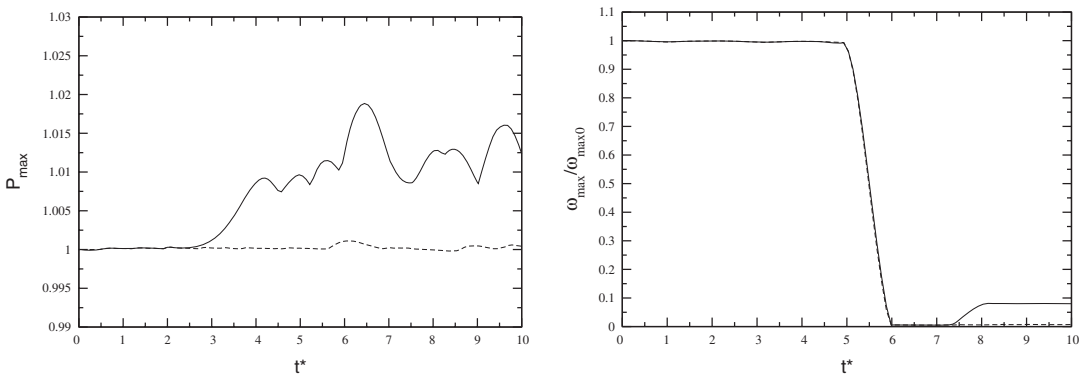

Figure 11. Time evolution of the maximum pressure and vorticity. Solid line: classical condition; dashed line: Giles condition.

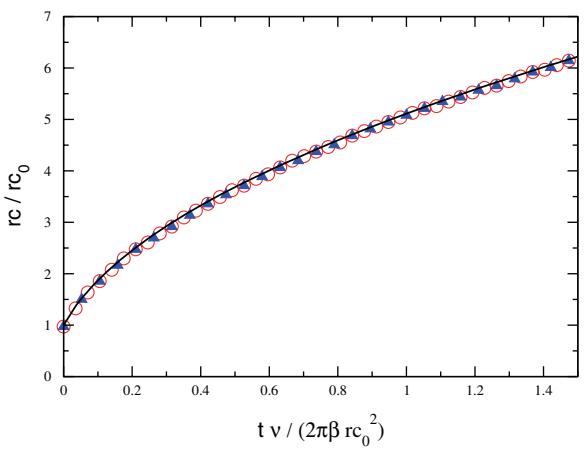

Figure 12. Evolution of vortex core radius of an isolated vortex by diffusion. Solid line: theoretical law, ○: without artificial dissipation and ▲: with artificial dissipation.

where ν is the kinematic viscosity, r_c the initial vortex radius and $\beta = 1.12^2$. In Figure 12, the theoretical law (Equation (48)) is compared with two simulations, one being performed with artificial dissipation and the other without dissipation. The value of the free coefficient in the artificial dissipation is taken equal to 0.002. There is a very good agreement between the numerical results and theory, the artificial dissipation has no major effect on the diffusion process of an isolated vortex.

For the second aspect (ii), three-dimensional temporal simulations were performed following the work of Le-Dizes and Laporte [26]. They studied the merging process of two co-rotating vortices by the development of a short-wavelength elliptic instability (Figure 13(a)), following the methodology supported by temporal direct numerical simulations (periodic BCs were imposed in

DOI: 10.1002/fld

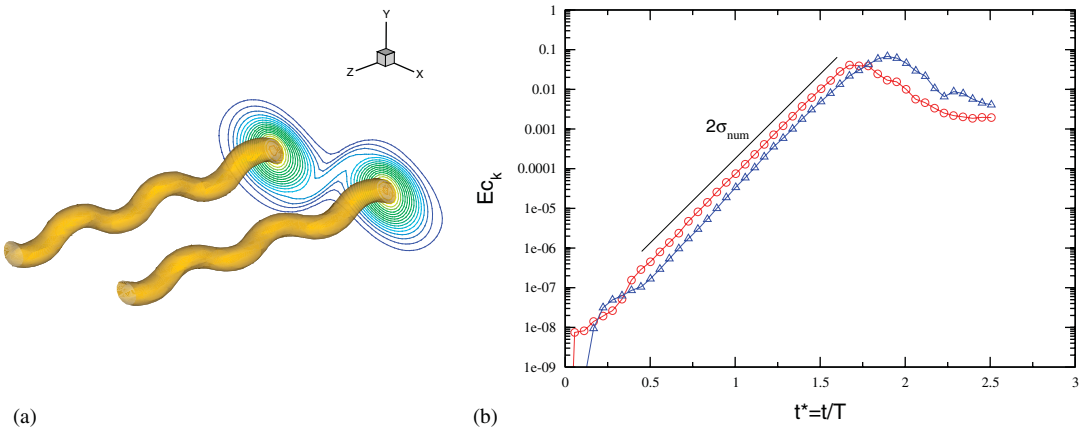

Figure 13. Elliptic instability in a co-rotating vortex system by temporal DNS. (a) Selected vorticity isosurface $|\omega| = 0.8|\omega_{\max}|$ at the time $t^* = t/T = 1.56$ where $T = 2\pi^2 d_0^2/\Gamma$ is the turnover period of the vortex system and (b) history time of the kinetic energy of the unstable mode: ∘ without artificial dissipation and △ with artificial dissipation.

the axial direction). Here, we analyse only the growth rate of the unstable mode, which dominates the dynamics, following its kinetic energy time evolution.

The initial condition consists of a co-rotating vortex system with a small perturbation corresponding exactly to three wavelengths of elliptic instability. To that end, a sinusoidal law is imposed on one velocity component of one vortex with a very small amplitude $A = 0.005V_0$ (here $V_0 = 0.1$ is the maximum vortex azimuthal velocity). The axial domain length is $L = 3\lambda$ where λ is the wavelength of the most unstable mode predicted by the formulation of Le-Dizes and Laporte. To calculate its kinetic energy, a Fast Fourier Transform is performed in the axial direction (details in Laporte and Corjon [27], Section C). The Reynolds number based on the circulation is $Re_\Gamma = 10^4$. The time evolution of the kinetic energy of the unstable mode is plotted in Figure 13. The dissipation does not modify the unsteady three-dimensional dynamics. The instability growth rate σ_{num} is identical for the two simulations with and without artificial dissipation. However, as expected, the kinetic energy level is slightly lower for the case with artificial dissipation, but only during the linear phase of the instability development. The predicted value of the instability growth rate can be compared with this theoretical value, and a difference of only $\sim 8\%$ is obtained [26].

6. FIRST VALIDATION: VORTEX BREAKDOWN

This section presents the validation of the numerical tool to simulate the spatial development of a vortex. Indeed, the approach often employed to simulate an aircraft wake vortex is the temporal approach. It is based on the assumption that the axial flow gradients can be neglected in comparison to the transverse ones. However, a strong phenomenon responsible for a wake vortex decay is the so-called vortex breakdown ([25, 28, 29] and therein) where the axial gradients play an important role. This physical phenomenon is characterized by a re-circulation zone in the vortex core, which both its form and size are dependent to the characteristic flow parameters. Vortex breakdown has inspired

DOI: 10.1002/fld

many investigations as it is encountered in many flow types (aerodynamics, combustion, etc.) and presents different characteristics (number of stagnation points and re-circulation regions, steady and unsteady states, etc.). Our goal is not to analyse this phenomenon but to use it as a validation exercise for the spatial evolution of a vortex flow. A simulation identical to the one of Ruith *et al.* [29] is reproduced. They analysed the vortex breakdown by DNS regarding the three-dimensionality and unsteadiness effects with respect to the existence of this phenomenon.

Two flow configurations have been chosen to compare our simulation to the results of [29]. The first one corresponds to an axisymmetric steady vortex breakdown and the second one to an unsteady case. These cases are characterized, respectively, by a ratio between the free stream axial and azimuthal velocities, $S=v_\theta/W=0.8944$ and $S=1.095$ (without axial velocity deficit in the vortex core). The Reynolds number is $Re=Wr_c/\nu=200$ based on the free stream axial velocity W, the vortex core radius r_c and viscosity ν. The initial condition is obtained from a Grabowski profile and consists in a single tubular vortex placed at the centre of the computational domain which is a square with a side length of $30r_c$. In the transverse xy-directions the mesh is regular in a square box around the vortex with a resolution of $\Delta_x=\Delta_y=0.1r_c$. The grid is stretched towards the boundaries and regular in the axial z-direction with $\Delta_z=0.1r_c$. For the inflow condition, the three velocity components and the temperature are imposed. This is similar to a value of the parameter α equal to 1 (Equation (22)).

The steady axisymmetric vortex breakdown is illustrated in the Figure 14, where a selected isosurface and isocontours of vorticity in the first plane are plotted. It can be observed that the vortex breakdown for this flow configuration ($S=0.8944$) is characterized by a small bubble of vorticity with an internal stagnation point. Ruith *et al.* [29] found a steady vortex breakdown for this configuration, which is also obtained in our simulation, as shown by the axial velocity profiles in the longitudinal direction at different times (Figure 14(b)).

Ruith *et al.* [29] show that for the second configuration with $S=1.095$ and $Re=200$, the vortex breakdown reaches a quasi-steady state, before becoming unstable and unsteady. These

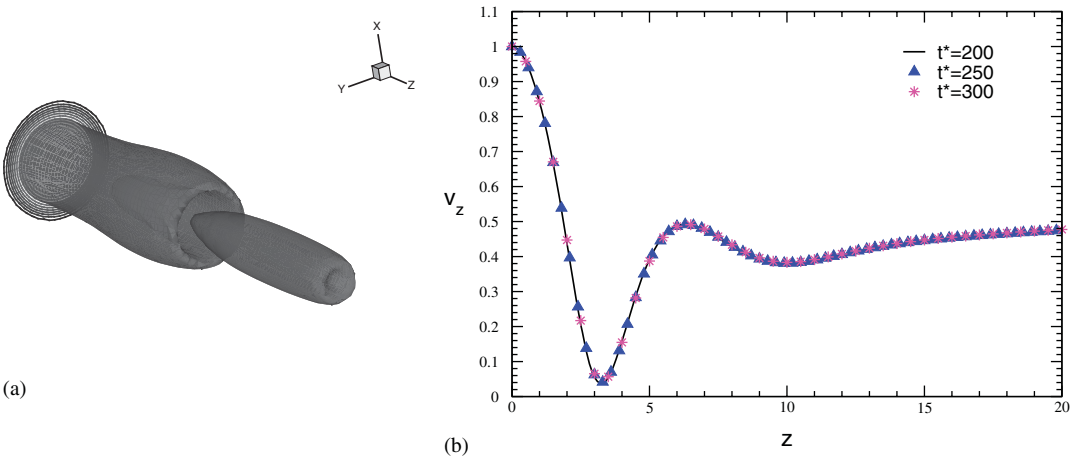

Figure 14. Steady vortex breakdown for the case $S=0.8944$ and $Re=200$. (a) Selected isosurface of vorticity $|\omega|=0.5|\omega_{max}|$ and vorticity isocontours in the first plane and (b) axial velocity profiles in longitudinal direction at different time $t^*=t/(r_c/W)$.

DOI: 10.1002/fld

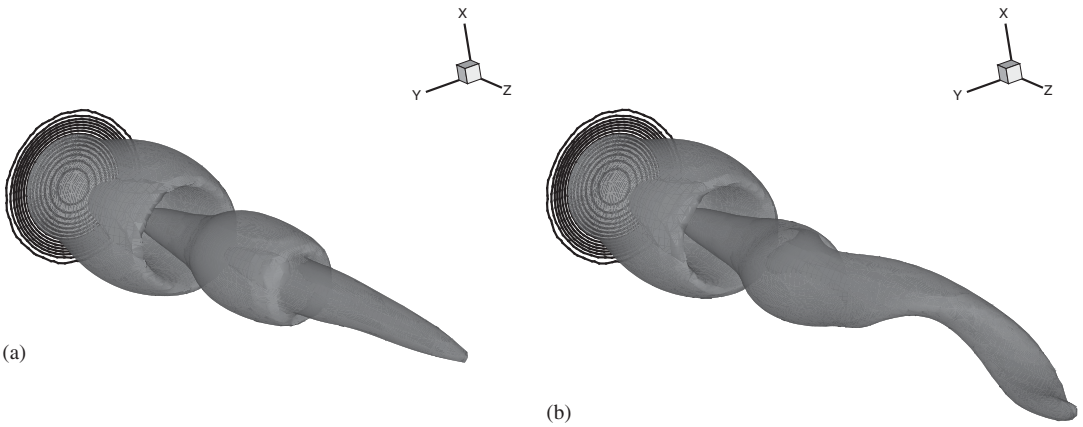

Figure 15. Vortex breakdown for the case $S=1.095$ and $Re=200$. Visualization of a selected vorticity isosurface $|\omega|=0.4|\omega_{\max}|$: (a) quasi-steady state at $t^*=t/(R/U)=100.4$ and (b) unsteady state at $t^*=t/(R/U)=164.4$.

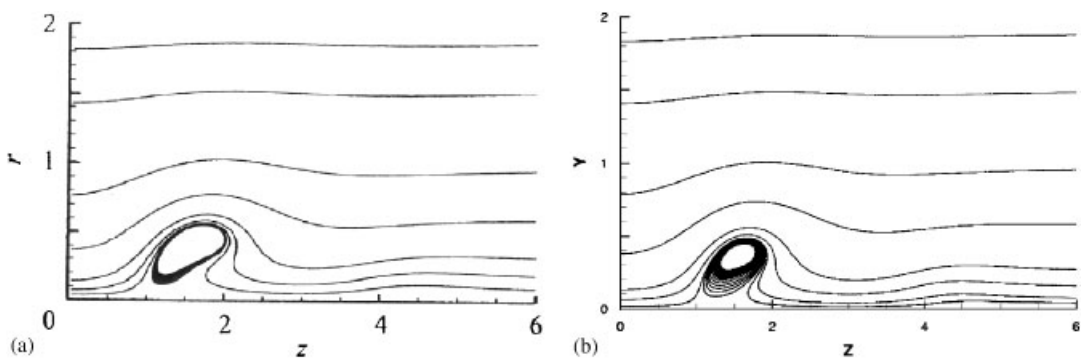

Figure 16. Projected streamlines in the median plane for the axisymmetric quasi-steady vortex breakdown: (a) from Ruith *et al.* [29] (by courtesy JFM) and (b) present result.

two states are illustrated in Figure 15 for a selected constant vorticity isosurface at two different times. The unsteadiness character is marked by an helical form behind the vortex breakdown. The quasi-steady state allows comparing our results with the ones of Ruith *et al.* The streamlines are plotted in Figure 16 for the two simulations; there is a good agreement for the position and size of the re-circulation zone. This agreement is also observed in the axial velocity profiles in longitudinal direction plotted on Figure 17. The differences of the vortex breakdown shape and axial velocity peaks (at $z=3$, a difference of 20%) can be explained by our approximation of axisymmetric vortex flow on a Cartesian mesh and by the fact that the second-order difference finite scheme employed by Ruith *et al.* is more dissipative than our scheme (sixth-order compact scheme). Moreover, it is difficult to find the quasi-steady state, which seems to be dependent on the numerical schemes. This comparison allows us to be confident in our numerical tools to reproduce, applying appropriated BCs, a spatial development of vortex flow. The next section presents the

DOI: 10.1002/fld

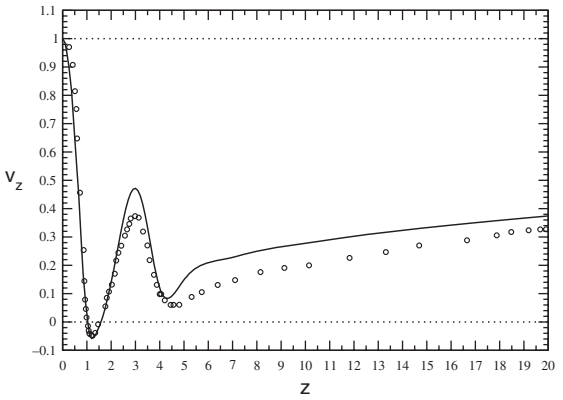

Figure 17. Axial velocity profiles along the vortex core in the longitudinal direction. Solid line: present result and ○: points extracted from the simulation of Ruith *et al.* [29].

final application: spatial simulation of three-dimensional unstable merging of a co-rotating vortex system.

7. SPATIAL SIMULATION OF VORTEX MERGING

The physical merging phenomenon of a co-rotating vortex system [24] can take place either under stable conditions or through the development of a short-wavelength elliptic instability, called unstable merging. The stable merging dynamics is essentially two-dimensional whereas the elliptic instability implies thre-dimensional considerations. The dynamics of such instabilities is characterized by an oscillation of the vortex core position in the axial direction. For saturating instability, the flow becomes pseudo-turbulent leading to a disturbed final vortex, obtained by a re-organization of the turbulent structures due to the global rotational motion. Here, we proposed to simulate the spatial development of such an instability by DNS. The fundamental goal of the spatial simulation is to take into account the axial velocity, and thus to show and determine its influence on the short-wavelength elliptic instability. Lacaze *et al.* [30] show by a theoretical stability analysis of a Batchelor vortex model (a Lamb–Oseen vortex + axial velocity) that other unstable modes of elliptic instability can develop in the vortex due to the axial velocity. The following two paragraphs deal with the computational set-up and the first quantitative analysis.

7.1. Computational set-up

Three vortex systems have been considered with various ratio of axial and azimuthal velocity, as summarized in Table I. All calculations are initialized identically, and using the same BCs and mesh grid resolution.

The inflow BC detailed in Section 3.3 requires the knowledge of transverse velocity components. The latter are obtained by a first two-dimensional temporal simulation in order to obtain a preliminary solution to the NS equations (as the superposition of two vortices is not a solution). To that end, two Lamb–Oseen vortices are placed in the domain centre with the identical circulation

DOI: 10.1002/fld

Table I. Summary of three-dimensional spatial simulations of co-rotating vortex pair.

Configuration	1	2	3
Domain L_x, L_y, L_z	$120*120*420$	$120*120*400$	$100*100*500$
Mesh nx, ny, nz	291, 291, 1401	291, 291, 1301	241, 241, 2001
V_0/W at $z=0$	1.55	0.62	0.32
q at $z=0$	1.38	12.97	5.02

V_0 is the maximum azimuthal velocity, W the free stream axial velocity and $q=1.569*V_0/(W-W_c)$ is the swirl number (W_c is the axial velocity at the vortex centre).

Γ and core size r_c, and a separation distance d_0. The Reynolds number based on the circulation is $Re_\Gamma = 10^4$. The computational domain is initialized by duplicating the two-dimensional velocity field into each axial plane, added to a constant free stream axial velocity $W = 0.2$. Note that this velocity determines the stagnation pressure at the inflow condition. A first simulation is performed to reach a time converged solution.

The computational domain is represented in Figure 1 and the dimensions are summarized in Table I. In the xy-directions, the mesh is regular in the region of the vortex dynamics interest (resolution $\Delta_{x,y} = 0.15 r_c$) and then stretched towards the boundaries. It is regular in the axial direction with a resolution of $\Delta_z = 0.3 r_c$. The main difficulty is to correctly estimate the axial length necessary to capture the complete merging process. Indeed, this is the highest constraint to perform spatial three-dimensional evolution of a vortex system. Preliminary two- and three-dimensional temporal simulations have been performed to analyse the merging process without axial velocity for the vortex systems considered here. These results showed that a range of axial domain lengths can be identified to simulate the complete merging process of co-rotating vortices, using the transformation $L_z = W*t$. Moreover, the theoretical prediction of Le-Dizes and Laporte [26] for a Lamb–Oseen vortex system without axial velocity has been used to determine the different instability wavelengths λ. For the vortex systems considered here, the instability wavelength of the most unstable mode is close to $\lambda \sim 3 r_c$. We assumed that the wavelengths of elliptic instabilities with axial flow are close to the ones without axial flow. To capture the spatial development of such instabilities, an axial resolution of 10 grid points per wavelength has been chosen and seems to be enough. It leads to a very large number of grid points (Table I). We performed massively parallel computations on an IBM 'Blue Gene', using 1024 processors and each configuration required a total CPU time of 516000 h.

When a time converged solution is obtained, a small perturbation is added to the transverse velocity components at the bottom face in order to trigger the instability development. The magnitude of the perturbations is calculated by a random value varying in time close to $10^{-4} V_0$. This perturbation corresponds to small displacements of the vortex core position, as it is a known effect of development of short-wavelength elliptic instability. More precisely, a vorticity perturbation is added at the inflow plane around each vortex core, which acts like a small displacement of a Lamb–Oseen vortex as:

$$\omega' = (\varepsilon_1 \cos\theta + \varepsilon_2 \sin\theta) \exp\left(-\frac{r^2}{b'^2}\right) \tag{49}$$

where ε_1 and ε_2 are small random numbers and b' adjusts the size of the perturbed area (here $b' = 2 r_c$). Through the integration of the Biot and Savart law, an analytical formulation can be established for the resulting perturbation velocities.

DOI: 10.1002/fld

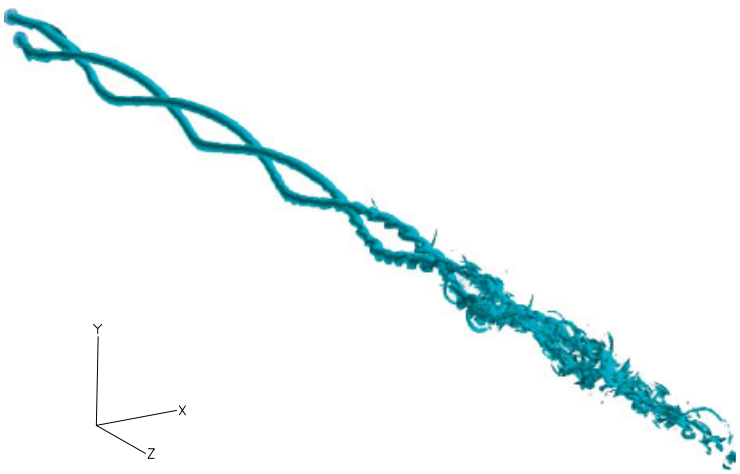

Figure 18. Configuration 1: spatial evolution of co-rotating vortices through the development of short-wavelength instability illustrated by a selected isosurface of vorticity magnitude $|\omega| = 0.23|\omega_{\max}|$.

7.2. Computational results

Configuration 1 is presented in Figure 18. It can be observed that the tubular vortices are deformed very close to the inflow condition, corresponding to the consequences of the instability development. When the instability saturates, the flow becomes turbulent and the large vorticity structures are re-organized into a final disturbed vortex due to the global rotational motion. This result shows that the vortex deformations are elongated in the longitudinal direction due to the axial velocity, contrary to a temporal simulation without axial velocity (Figure 13). In the latter case, the elliptic instability is known to result from the resonance of the two Kelvin modes $m = -1$ and 1 [24]. With axial velocity, these modes can be damped and new modes (e.g. $m = -2$ and 0) can be excited [30]. The vortex structure deformations seem to result from the amplification of these new modes since their consequences are different from the ones observed and clearly identified in the temporal approach without axial flow. This preliminary physical analysis must be continued to determine precisely how the merging process is affected by the development of these new modes.

The instability amplification is quantified by plotting the variance of the cross-flow and axial kinetic energy as represented in (Figure 19(b)). These quantities are integrated in each transverse plane. It must be noticed that all results presented here correspond to a statistical converged state. This means that the mean or the variance of the velocity component for example does not vary when the number of time iteration increases.

The flow is laminar and no instability is yet amplified close to the inflow plane (Figure 19(b)). Beyond the downstream distance $z = 50r_c$, the variance increases strongly to reach a saturation level, corresponding to the distance where the merging of the co-rotating vortices starts. The time averaged vortex centre positions, localized by a vorticity extremum, are plotted in Figure 19(a). The rotational motion of one vortex around the other is well illustrated. It can be observed that the vortex system deviates from the domain centre. It can be noticed that this drift was observed only when a perturbation is injected at the inflow plane. For all simulations presented here, it has been verified that the vortex system and the final vortex remain in the regular transverse domain where the resolution is fine (domain $L_x * L_y = 25 * 25$).

DOI: 10.1002/fld

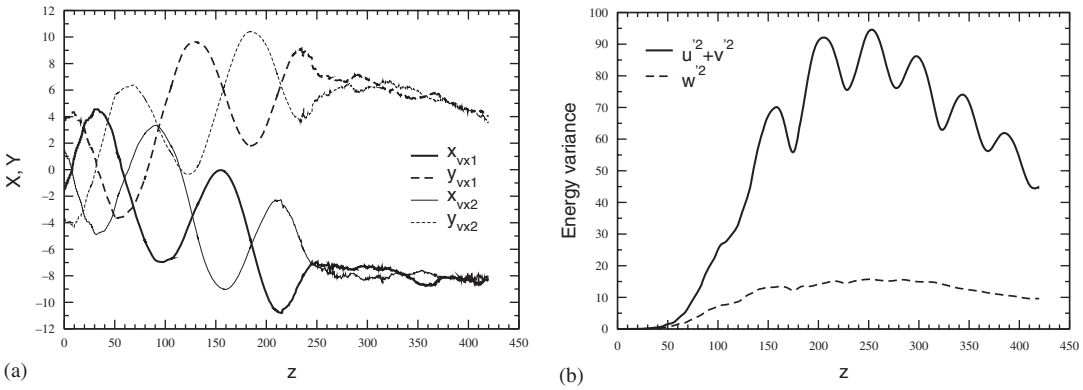

Figure 19. Configuration 1: (a) transverse vortex centre positions as function of the axial distance and (b) variance of the cross-flow and axial kinetic energy.

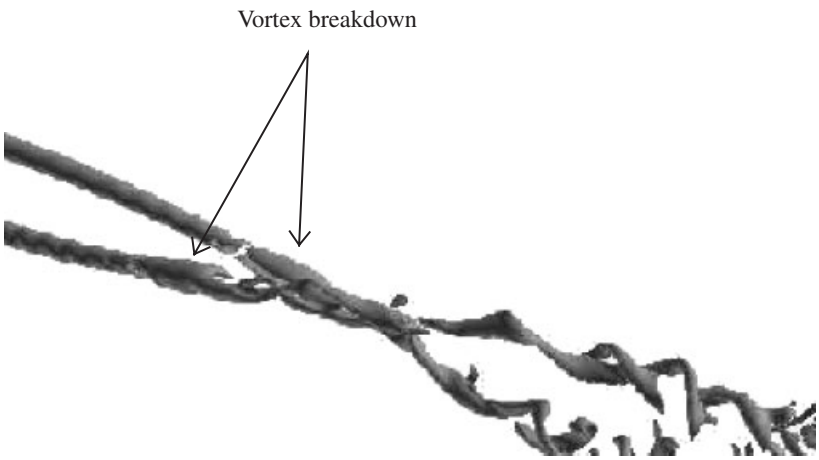

Figure 20. Configuration 2: selected isosurface of vorticity magnitude.

The results of the vortex flow configuration 2 is illustrated in Figure 20. The spatial dynamics is marked by a sudden and drastic change while the elliptic instability have started to be amplified (small oscillations of the vortex shapes). This physical phenomenon is called vortex breakdown (see Section 6) and leads to the formation of a bubble followed by a wake characterized by large helical structures. A reorganization of these structures into a single vortex can take place due to the global rotational motion (axisymmetrization process).

For configuration 3, which is characterized by the smallest ratio of the velocity peaks, no vortex breakdown is observed instead a spatial development of an elliptic instability (Figure 21) such as configuration 1. Nevertheless, the axial velocity effects are smaller and the vortex deformations are similar to those obtained by temporal simulations (Figure 13) with well-separated vortices. From the axial position $z \sim 200$, small oscillations of the vortex shape is observed. A spatial growth of these oscillations occurs and leads to an exchange of vorticity between the two vortices, and

DOI: 10.1002/fld

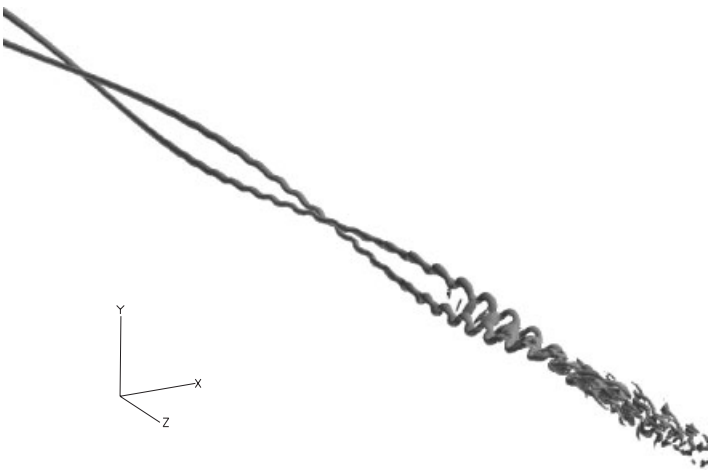

Figure 21. Configuration 3: selected isosurface of vorticity magnitude.

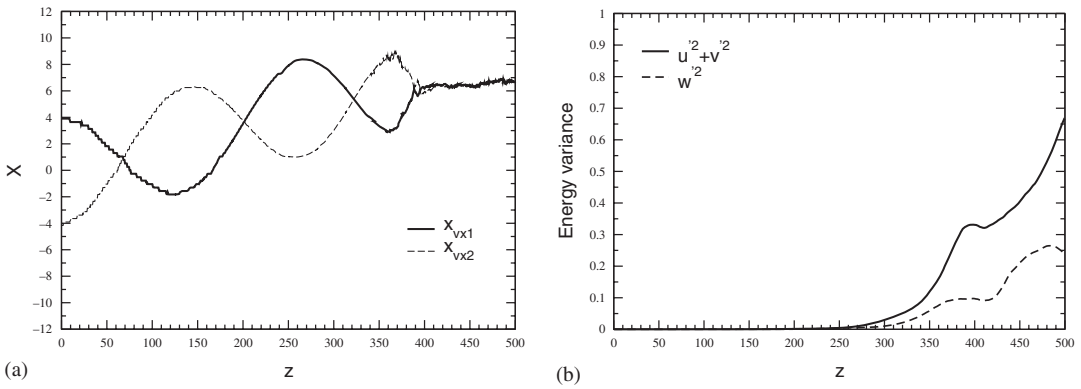

Figure 22. Configuration 3: (a) horizontal vortex centre positions as function of the axial distance and (b) variance of the cross-flow and axial kinetic energy.

finally to the merging. The spatial evolution of the kinetic energy variance traduces this growth of perturbations (Figure 22) until the instability saturation. The two vortices merge at the downstream distance $z \sim 380$ just before the end of the computational domain.

8. CONCLUSIONS AND FUTURE WORK

The present numerical study has been elaborated with the objective to simulate the spatial evolution of a co-rotating vortex system through the development of short-wavelength elliptic instabilities, which leads to the merging of the two vortices. The main difficulties arise from the different characteristic lengths of the flow: vortex size, instability wavelength and domain axial length to

DOI: 10.1002/fld

capture the complete merging process; and also from the capacity of the boundary conditions (BCs) to represent such vortex flow and to suppress numerical wiggles. Thus, the BCs were adapted to simulate the spatial evolution of vortex flow with non-zero total circulation. Three vortex flow configurations were simulated, characterized by different swirl numbers. This parameter can be defined simply by the velocity ratio S between the maximum azimuthal and axial velocity, or by the one used in the stability analysis q (as defined in Table I).

The proper choice of the inflow configuration is crucial as different vortex dynamics can take place in spatial simulations due to the effects of axial velocity, such as vortex breakdown, development of helical instability or short-wavelength instability with new unstable modes. If the inflow swirl number is lower than $|q|<1.5$, each vortex can become unstable through the development of helical instability [31]. If the velocity peak ratio S reaches a critical value in the approximative range of $[0.89, 1.4]$ at a downstream distance, the vortex breakdown [25] can dominate the vortex dynamics even if some elliptic unstable mode are already excited. If large swirl numbers are used, the curvature of the vortex system becomes very elongated and the simulation of the complete merging process cannot be ensured due to the choice of computational domain and since very important computational resources are required unlike for temporal simulations. In spatial simulations it is very difficult to isolate one physical phenomenon, which makes these spatial simulations more complex to be physically analysed. For the vortex systems considered here, our preliminary results show that the axial velocity can modify the development of short-wavelength instability. However, further physical analysis are required. In particular, a detailed comparison of the results of the three configurations will be conducted by performing a Fourier series development in transverse planes around each vortex core to characterize the vortex perturbation shape during the development of short-wavelength instability.

In order to fully benefit from the spatial simulations, we will take into account the possible development of convective or absolute instability but also the curvature of the vortex system, or more generally, the three-dimensional effects, which can play a major role in the nonlinear dynamics of vortex system.

ACKNOWLEDGEMENTS

The results presented in this paper are obtained from research conducted within the European project 'FAR-Wake' (Fundamental Research on Aircraft Wake Phenomena), AST-CT-2005-012238. The corresponding financial support of the European Union is gratefully acknowledged. The authors would also like to gratefully acknowledge P. Brancher (IMFT-Toulouse) and J. F. Boussuge (CERFACS) for their support and suggestions.

REFERENCES

1. Cerretelli C, Williamson CHK. The physical mechanism for vortex merging. *Journal of Fluid Mechanics* 2003; **475**:41–77.
2. Ferreira de Sousa JSA, Pereira JCF. Reynolds number dependence of two-dimensional laminar co-rotating vortex merging. *Theoretical and Computational Fluid Dynamics* 2005; **19**:65–75.
3. Orlandi P. Two-dimensional and three-dimensional direct numerical simulation of co-rotating vortices. *Physics of Fluids* 2007; **19**:013101-1–013101-18.
4. Thompson KW. Time dependant boundary conditions for hyperbolic systems—part 2. *Journal of Computational Physics* 1990; **89**:439–461.
5. Giles MB. UNSFLO: a numerical method for unsteady inviscid flow in turbomachinery. *GTL Report 195*, MIT Gas Turbine Laboratory, 1988.

DOI: 10.1002/fld

6. Tam C, Dong Z. Radiation and outflow boundary conditions for direct computation of acoustic and flow disturbances in a nonuniform mean flow. *Journal of Computational Acoustics* 1996; **2**(4):175–201.
7. Bayliss H, Turkel E. Far field boundary conditions for compressible flows. *Journal of Computational Physics* 1982; **48**:182–199.
8. Rudy DH, Strikwerda JC. A non-reflecting outflow boundary condition for subsonic Navier–Stokes calculations. *Journal of Computational Physics* 1980; **36**:55–70.
9. Poinsot TJ, Lele SK. Boundary conditions for direct simulations of compressible viscous flows. *Journal of Computational Physics* 1992; **101**:104–129.
10. Hernandez G. Contrôle actif des instabilités hydrodynamiques des écoulements subsoniques compressibles. *Ph.D. Thesis*, CERFACS, 1996.
11. Colonius T. Modeling artificial boundary conditions for compressible flow. *Annual Review of Fluid Mechanics* 2004; **36**:315–345.
12. Blaidsell GA, Spyropoulos ET, Qin JH. The effects of the formulation of nonlinear terms on aliasing errors in spectral methods. *Applied Numerical Mathematics* 1996; **21**:207–219.
13. Lele SK. Compact finite difference schemes with spectral-like resolution. *Journal of Computational Physics* 1992; **103**:16–42.
14. Gamet L, Ducros F, Nicoud F, Poinsot T. Compact finite difference schemes on non-uniform meshes. Application to direct numerical simulation of compressible flows. *International Journal for Numerical Methods in Fluids* 1999; **29**:159–191.
15. Yoo CS, Wang Y, Trouve A, Im HG. Characteristic boundary conditions for direct simulations of turbulent counterflow flames. *Combustion Theory and Modelling* 2005; **9**(4):617–646.
16. Moet H, Laporte F, Chevalier G, Poinsot T. Wave propagation in vortices and vortex bursting. *Physics of Fluids* 2005; **17**:54–109.
17. Giles MB. Non-reflecting boundary conditions for Euler equation calculations. *AIAA Journal* 1990; **28**(12): 2050–2058.
18. Bruneau CH, Creuse E. Towards a transparent boundary condition for compressible Navier–Stokes equations. *International Journal for Numerical Methods in Fluids* 2001; **36**:807–840.
19. Barone MF. Receptivity of compressible mixing-layer. *Ph.D. Thesis*, Stanford University, May 2003.
20. Uzun A, Blaisdell GA, Lyrintzis AS. 3-D large eddy simulation for jet aeroacoustics. *9th AIAA/CEAS Aeroacoustic Conference*, Hilton Head, SC, 2003. AIAA-2003-3322.
21. Bogey C, Barre S, Bailly C. Direct computation of the noise generated by a hot coaxial jet. *13th AIAA/CEAS Aeroacoustic Conference*, Rome, Italy, 2007. AIAA-2007-3587.
22. Bogey C, Bailly C. Three-dimensional non reflective boundary conditions for acoustic simulations: far-field formulation and validation test cases. *Acta Acoustica* 2002; **88**(4):463–471.
23. Tam CK, Webb JC. Dispersion-relation-preserving finite difference schemes for computational acoustics. *Journal of Computational Physics* 1993; **107**:262–281.
24. Meunier P, Le-Dizes S, Leweke T. Physics of vortex merging. *Comptes Rendus Physique* 2005; **6**(4–5):431–450.
25. Billant P, Chomaz J-M, Huerre P. Experimental study of vortex breakdown in swirling jets. *Journal of Fluid Mechanics* 1998; **376**:183–219.
26. Le-Dizes S, Laporte F. Theoretical prediction for elliptical instability in a two-vortex flow. *Journal of Fluid Mechanics* 2002; **471**:169–201.
27. Laporte F, Corjon A. Direct numerical simulations of the elliptic instability of a vortex pair. *Physics of Fluids* 2000; **12**:1016–1031.
28. Leibovich S. The structure of vortex breakdown. *Annual Review of Fluids Mechanics* 1978; **10**:221–246.
29. Ruith MR, Chen P, Meiburg E, Maxworthy T. Three-dimensional vortex breakdown in swirling jets and wakes: direct numerical simulation. *Journal of Fluid Mechanics* 2003; **486**:331–378.
30. Lacaze L, Ryan K, Le-Dizes S. Elliptic instability in a strained Batchelor vortex. *Journal of Fluid Mechanics* 2007; **577**:341–361.
31. Mayer EW, Powell KG. Viscous and inviscid instabilities of a trailing vortex. *Journal of Fluid Mechanics* 1992; **145**:91–114.

DOI: 10.1002/fld